Nanoscale Advances

ROYAL SOCIETY OF CHEMISTRY

REVIEW

View Article Online
View Journal

Cite this: DOI: 10.1039/d5na00954e

Environmental classification of synthetic methods for zinc oxide nanoparticles: a comparative review of sustainable green and conventional approaches with their diverse applications

Mohga Basseem, *[a] Mohamed A. Salem,*[b] Islam Ibrahim,*[cd] George V. Belessiotis, [e] Sobhi M. Gomha, [f] Magdi E. A. Zaki[g] and Ahmed Ragab *[hd]

Nanotechnology has significantly advanced the field of materials science, with zinc oxide nanoparticles (ZnO NPs) emerging as versatile materials owing to their unique physicochemical properties, biodegradability, and tunability. These features make them promising candidates for various biomedical and environmental applications. This review summarizes the literature on ZnO NPs, with a particular emphasis on environmental considerations. Conventional chemical synthesis methods, including sol–gel, emulsion, hydrothermal, solvothermal, precipitation, co-precipitation, and mechanochemical techniques, facilitate precise control over particle size and morphology; however, they frequently require the use of toxic reagents. Compared with green synthesis methods, these methodologies offer enhanced repeatability, crystallinity, and performance in photocatalytic and sensing applications; however, they impose a greater environmental burden. In contrast, the use of plant extracts and microorganisms for green synthesis offers a viable alternative for producing safer, more sustainable ZnO nanoparticles. Although bio-assisted reduction and the application of natural capping agents have improved biocompatibility and surface functionality, these methods continue to face significant challenges. Key issues include limited control over the particle size distribution, uniformity of morphology, and batch-to-batch reproducibility, all of which can negatively impact the consistency and functional performance of nanoparticles. Furthermore, characterization techniques are essential for understanding NP properties. XRD confirms crystallinity and estimates particle size (Scherrer equation), whereas SEM and TEM reveal morphology and shape variations, including spheres, cubes, rods, hexagonal flowers, and nanotubes. EDX can be used to determine the elemental composition, XPS can be used for surface chemical analysis, UV-Vis can be used to determine optical properties and band gap, and FT-IR can be used to detect functional groups and biomolecule capping in green synthesis. BET analysis is done to measure surface area, and the zeta potential is used to assess surface charge and stability. The applications of ZnO NPs encompass a wide range of fields, including photodegradation, photosensing, electrochemical catalysis, gas sensing, chemical detection, photocatalysis, agriculture, and biomedicine. Given the importance of both performance and sustainability, future research should prioritize hybrid approaches that integrate the precision of chemical synthesis with the ecological advantages of green methodologies, such as biosynthesis coupled with controlled thermal treatment.

Received 8th October 2025
Accepted 24th May 2026

DOI: 10.1039/d5na00954e

rsc.li/nanoscale-advances

[a]Chemistry Department, Faculty of Science, Al-Azhar University (Girls), Nasr City, Cairo, Egypt. E-mail: mohga_basseem@azhar.edu.eg

[b]Health Specialties, Basic Sciences and Their Applications Unit, Applied College, Muhayl Asir, King Khalid University, Abha 62529, Saudi Arabia. E-mail: masalem@kku.edu.sa

[c]Department of Chemistry and Biochemistry, Florida International University, Miami, FL 33199, USA. E-mail: Ihussein@fiu.edu

[d]Chemistry Department, Faculty of Science (Boys), Al-Azhar University, 11884 Nasr City, Cairo, Egypt. E-mail: ahmed_ragab@azhar.edu.eg

[e]School of Electrical Engineering, National Technical University of Athens, 9 Iroon Polytechniou St., 15780 Zografou, Athens, Greece

[f]Department of Chemistry, Faculty of Science, Islamic University of Madinah, Madinah, 42351, Saudi Arabia

[g]Department of Chemistry, College of Science, Imam Mohammad Ibn Saud Islamic University (IMSIU), 11623 Riyadh, Kingdom of Saudi Arabia

[h]Chemistry Department, Faculty of Science, Galala University, Galala City, Suez, 43511, Egypt. E-mail: ahmed.abdelwahab@gu.edu.eg; ahmed_ragab7@ymail.com

1 Introduction

Zinc oxide nanoparticles have garnered significant attention because of their exceptional physicochemical properties, including high thermal stability, catalytic activity, antibacterial efficacy, and ultraviolet-blocking capabilities. These properties make them suitable for a diverse range of applications, such as photocatalysis,[1] environmental remediation,[2] optical electronics,[3] skincare formulations,[4] drug delivery systems,[5] and various biomedical applications.[6] However, as the production and utilization of ZnO nanoparticles increase, there is growing concern regarding the implications of their fabrication processes for environmental integrity and human health.[7] Consequently, a critical area of focus within nanotechnology research is the development of sustainable and environmentally benign methods for synthesizing ZnO nanoparticles.[8]

From the environmental perspective, the synthesis route is crucial in determining the overall sustainability of ZnO nanoparticles. Traditional chemical synthesis processes, while effective in achieving precise control over particle size, shape, and crystallinity, often pose significant environmental challenges. These challenges include the use of toxic chemical precursors, hazardous organic solvents, excessive energy consumption, and the generation of chemical waste, all of which threaten ecosystems and human health. As the scale of ZnO nanoparticle manufacturing continues to grow, these issues raise serious concerns about the long-term environmental impact of current synthesis methods. Consequently, it has become essential to analyze and categorize ZnO nanoparticle synthesis methods on the basis of their environmental impact, underscoring the urgent need for a greater focus on green and eco-friendly synthesis strategies. Additionally, the development of green synthesis over traditional chemical processes has several benefits, including cost-effectiveness, ease of scalability for large-scale nanoparticle manufacturing, and environmental friendliness. Furthermore, green synthesis is often safer and more environmentally friendly because it does not require high temperatures, high pressures, excessive energy input, or hazardous chemicals.[9] Based on their environmental impact, ZnO nanoparticle synthesis methods can be classified into two categories: green (eco-friendly or biological) methods and chemical (conventional) methods.[10] Each category encompasses a range of techniques that vary in terms of reagents, reactions, scalability, toxicity, and energy requirements. This classification framework facilitates an understanding of how different synthesis strategies correlate with the principles of green chemistry and how nanomaterials can be produced sustainably.[11,12]

Furthermore, in terms of green synthesis, also referred to as biological or eco-friendly synthesis, natural and renewable resources, including plant extracts and microorganisms (such as bacteria, fungi, and algae), are employed to produce zinc oxide (ZnO) nanoparticles. This methodology has gained increasing prominence due to its environmentally sustainable, biodegradable, and safe attributes. Unlike traditional methods that utilize toxic chemicals or hazardous solvents, green synthesis typically operates at room temperature under elevated pressure conditions.[13,14] Moreover, microbial synthesis involves the use of bacterial or fungal cultures that act as stabilizing and bio-reducing agents. Through enzymatic activities and extracellular secretions, microorganisms such as *B. subtilis*, *A. niger*, and *P. chrysogenum* have been demonstrated to facilitate the synthesis of ZnO nanoparticles.[15–17] A comparable process is observed in plant-mediated synthesis, which employs phytochemicals (*e.g.*, flavonoids, alkaloids, and terpenoids) to reduce zinc salts into ZnO nanoparticles. In addition to their simplicity, cost-effectiveness, and scalability, plant-based methods offer substantial advantages over conventional approaches.[18] Additionally, one of the most significant positive environmental impacts of green synthesis can be described as

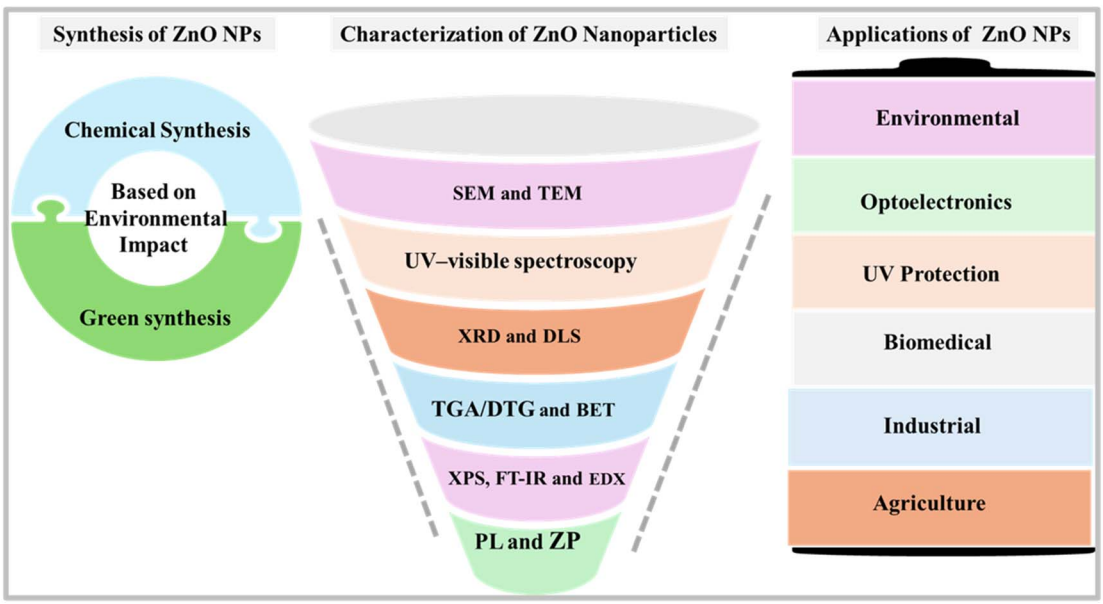

Fig. 1 Schematic diagram illustrating different methods for the synthesis of zinc oxide nanoparticles (ZnO NPs), along with their characterization and applications.

the reduction of hazardous waste and the utilization of benign solvents, such as water. Moreover, the ZnO nanoparticles produced are often treated with natural biomolecules, enhancing their biocompatibility and potential applications in the biomedical field. Nonetheless, challenges remain, including batch-to-batch variability, prolonged reaction times, and difficulties in achieving uniform particle morphology[19,20] (Fig. 1).

Furthermore, conventional techniques for the synthesis of zinc oxide (ZnO) nanoparticles predominantly employ chemical methods. These methods include sol–gel, emulsion, hydrothermal, solvothermal, precipitation, co-precipitation, and mechanochemical techniques.[21] Chemical synthesis typically involves the use of chemical reagents and solvents to facilitate particle formation and growth, utilizing metal salts as precursors. Compared with alternative methods, chemical processes exhibit high reproducibility and enable precise control over parameters such as particle size, shape, crystallinity, and purity, making them compatible with industrial-scale applications.[22,23] For example, the sol–gel method involves the hydrolysis and polycondensation of zinc alkoxides or salts to produce homogeneous ZnO nanoparticles.[24] Similarly, hydrothermal and solvothermal techniques allow for controlled crystallization and morphological modifications through high-temperature processes conducted within sealed vessels.[25] These methods can be optimized by adjusting the reaction time, temperature, and pH to yield the desired nanostructures, including rods, wires, or flower-like formations. However, chemical synthesis poses significant environmental challenges, including the generation of hazardous waste products, substantial energy consumption, reliance on organic solvents, and the use of toxic substances[19] (Fig. 1). The disposal of chemical waste raises concerns regarding human safety, environmental sustainability, and the potential hazards associated with residual solvents in the final product. Ultimately, a comparison between green and chemical synthesis methods reveals a distinct trade-off between environmental safety and synthetic precision. While chemical methods offer superior accuracy and scalability, green approaches adhere more closely to the principles of green chemistry, thereby mitigating ecological and health risks.[26] Future research will likely focus on hybrid methodologies that leverage the benefits of both chemical and green synthesis techniques.

Based upon previous findings and in the continuation of review articles on ZnO nanoparticles,[27–33] this review classifies the synthesis of ZnO nanoparticles into two primary categories: conventional chemical methods and eco-friendly or biological (green) methods. Initially, we illustrated chemical methods, which encompass sol–gel, emulsion, hydrothermal, solvothermal, precipitation, co-precipitation, and mechanochemical techniques. These methods facilitate precise control over particle size and morphology. Furthermore, the green synthesis approach employs plant extracts and microorganisms, offering a more environmentally sustainable alternative to produce ZnO nanoparticles with diverse morphologies. In addition, for each synthesis method, we present a comprehensive overview of the conditions utilized, the chemical processes involved, the analytical techniques employed by various authors for characterization, and the applications identified within the existing literature.

2 Methods of synthesis

Many synthetic methods have contributed to the synthesis of zinc oxide nanoparticles. In the current review, we classified the synthesis methods of ZnO based on environmental impact.

2.1 Chemical synthesis (conventional methods)

The chemical synthesis method involves the utilization of chemical reagents, solvents, and controlled conditions. This approach allows for precise control over particle size and morphology through various techniques, including sol–gel, emulsion, hydrothermal, solvothermal, precipitation, co-precipitation, and mechanochemical methods, as detailed in Table 1. Furthermore, the advantages and disadvantages associated with these chemical synthesis methods for the synthesis of ZnO nanoparticles are illustrated in Fig. 2.

2.1.1 Sol–gel method. The sol–gel method is widely used for producing metal-oxide nanoparticles because of its simplicity, reliability, repeatability, and mild processing conditions. Consequently, zinc oxide can be surface-modified with specific substances, increasing its properties and broadening its applications. Sol–gel processing has several advantages, including a high degree of purity, narrow particle size distribution, and low processing temperatures that result in a uniform nanostructure. In addition to these benefits, the sol–gel technique is among the most attractive methods. In the sol–gel method, methanol dissolves zinc acetate dihydrate to give ZnO NPs at room temperature. It is necessary to increase the pH of the solution by adding sodium hydroxide. At room temperature, the modified sols were stirred ultrasonically for 60 min. and then filtered. The filtrate was left to stand for 48 hs to finish the gelation and hydrolysis. The precipitation of white ZnO crystals was observed. To remove the starting components, the white precipitate was filtered, thoroughly washed with excess methanol, and dried for two hs at 120 °C. The sol–gel mechanism showed that zinc acetate dihydrate dissolves in methanol. At pH values higher than 7, acetate ions are hydrolyzed to produce zinc hydroxide due to the increased availability of hydroxyl ions. Upon ionization, zinc hydroxide forms Zn^{2+} cations and OH^- anions. The Zn–O–Zn bridges created by the polymerization of the hydroxyl complex eventually turn into ZnO. The pH of the starting solution affects the crystallinity and particle size of the ZnO powder. The size of the ZnO particles gradually increases as the pH of the reaction mixture increases from 6 to 9. These particles, however, disintegrate and recrystallize as ZnO nanocrystallites as the pH increases above 9. Fig. 3 depicts the mechanism of the sol–gel process.

Vignesh *et al.* synthesized zinc oxide (ZnO) nanoparticles *via* a sol–gel method. Characterization of the synthesized nanoparticles was conducted utilizing XRD and SEM. The XRD analysis confirmed that the synthesized pure zinc oxide nanoparticles had a crystallite size of 36 nm. SEM images show larger

Table 1 Chemical synthesis methods of ZnO nanoparticles, including precursors, synthesis conditions, key properties, and applications

No.	Method	Precursors	Synthesis conditions[a]	Properties[a]	Applications	Ref.
1	Sol–gel	Zinc nitrate hexahydrate and sodium hydroxide	Dr: overnight and Cal: 3 h, 500 °C	D was 36 nm with form of flocks	Antibacterial activity	34
2	Sol–gel	Zinc acetate dihydrate, oxalic acid using ethanol as solvent	Dr: 80 °C for 2 h, Cal: 4 h at 650 °C St: 30 min at 60 °C	D was 20 nm with uniform spherical	Photocatalytic degradation	79
3	Sol–gel	Zinc acetate dihydrate and polyvinylpyrrolidone (PVP)	Dr: at 60 °C, Cal: 1h at 600 °C, St: 1 h at ambient T	D was 45 nm, and M changed from platelets to rods	—	80
4	Hydrothermal	Zinc acetate dihydrate, citric acid and deionized water as solvent	Reaction: magnetic stirring at 40 °C, pH: 13, auto. (19 h, at 150 °C), Dr: 80 °C, 12 h	Hexagonal rods (<500 nm) to flower/rose (∼3–4 μm) and irregular nanoscale plates with increasing T (100–200 °C)	—	81
5	Hydrothermal	Zinc acetate dihydrate, citric acid monohydrate, and sodium hydroxide	First Opt.: different pH: 7.5–13.5, (auto. 160 °C, 12 h) Second Opt.: auto.:24 h, T: 100–200 °C, dried: 60 °C,24 h	Temperature effect: hexagonal rods (16.8 nm), flower-like structures (17.18–20.41 nm), rose/plate-like structures (36.9–56.2 nm), pH effect: hexagonal pellets (33.67–59.22 nm), irregular/small nanoparticles (18.98–41.10 nm)	—	82
6	Microwave-assisted synthesis	Zinc acetate dihydrate and potassium hydroxide	RM: at 180 W for 20 min Dr: at 80 °C for 24h Cal: at 400 °C for 2 h	D from 145 to 185 nm, with a hexagonal flower nanorod wurtzite structure	Gas sensing evaluation	82
7	Microwave-assisted synthesis	Zinc nitrate hexahydrate or zinc acetate dihydrate and hydrazine hydrate and ammonia	pH(11.5), RM(1): 510 W, 15 min (S A1) and 680 W – 10 min (S A2), RM(2): 150 W – 15 min (solution B), Dr: 100 °C – 2 h., Cal: 600 °C – 3 h	Needle-shaped particle, D 50–150 nm	—	83
8	Microwave-assisted synthesis	Zinc sulfate, potassium hydroxide, and sodium sulfide	St: for 30 min, RM: at 180 W for 2 min, Dr: at 60 °C for 2h	D is ∼25 nm, with spherical morphology	Photocatalytic degradation of aniline and formaldehyde	84
9	Precipitation method	Zinc nitrate and ammonium carbonate solution	Vigorous St, Dr: at 100 °C – 6 h Cal: at 300 °C for 3 h	D is 30 nm in hexagonal wurtzite structure	—	85
10	Precipitation method	Zinc nitrate hexahydrate, zinc acetate dihydrate, zinc sulphate heptahydrate, sodium hydroxide, polyvinyl alcohol, potassium hydroxide, and ethanol	Magnetic St:30 min −2 h at 60 °C Precipitation: at 160 °C – 10 h Cal: at 300 °C for 6 h	D is in the range 11–21 nm for green synthesis, and 30–40 nm for chemical precipitation methods	Antimicrobial	86
11	Precipitation method	Zinc acetate dihydrate as a zinc source, ethylene glycol (EG) as a solvent and polyvinyl pyrrolidone (PVP) as a chelating agent	pH: 12.7. Replaced 0.2 g PVP- EG Sol, with 0.3 or 0.4 g (solvent effect). Ref: for 30 min – 25 °C, T (60, 70 and 80 °C); Dr: at 70 °C for 3 h	D of spherical (13.0 ± 1.9 nm at 25 °C and 9.0 ± 1.3 nm at 80 °C)	—	87

Table 1 (*Contd.*)

No.	Method	Precursors	Synthesis conditions[a]	Properties[a]	Applications	Ref.
12	Solvothermal method	Trisodium citrate dihydrate, cerium chloride heptahydrate, zinc acetate dihydrate and ethylene glycol	Auto T: 200 °C for 10 h Cal: 500 °C for 2 h	Uniform cavities (9.0 nm) in CeO2–ZnO, with smaller pores (∼2.4 nm) in the walls	Gas sensor and in diagnosis of diabetes and chemical detection	88
13	Solvothermal method	Zinc nitrate hexahydrate, silver nitrate, platinum(II) acetylacetonate, sodium hydroxide, ethanol, and cetyltrimethylammonium bromide	T: room temp for 1h, auto T: 120 °C for 3 and 6h, Dr: 80 °C	D, ZnO (2.5–13.3 nm) nanowires, Ag (17.3–24.3 nm) and Pt around (6.3 nm) Ag/Pt: quasi-spherical particles M	Photocatalytic degradation	89
14	Solvothermal method	Zinc acetate dihydrate, ethanol, and potassium hydroxide	T: 60 °C for 3 h Dr: at room temp	Wurtzite structure; crystallite size 10.08 nm; particle size 7.4 ± 1.2 nm	—	90
15	Solvothermal method	Zinc acetate dihydrate, surfactants such as sodium dodecyl sulfate (SDS), polyvinylpyrrolidone (PVP), and polyethylene glycol (PEG, MW = 10 000), ethanol, and NaOH	T: at 110 °C for 10 h	SDS: hexagonal disks (300 nm edge, 200 nm thick) PVP: bilayer disks (6 μm edge, 4 μm thick) PEG: flower-like (3–4 μm) aggregation of nanorods (200 nm)	Photocatalytic degradation	91
16	Microemulsion synthesis	Lanthanum nitrate hexahydrate, cobalt(II) nitrate hexahydrate, citric acid, 1-pentanol, 2, 2, 4-trimethylpentane, hexadecyltrimethylammonium bromide (CTAB), and potassium hydroxide	St: 6h, Cal: at 923 K for 3 h	D is 100 nm with a spherical shape	Electrochemical catalytic activity	92

[a] D: Crystallite size, M: morphology, Opt.: optimization, auto.: autoclaving conditions, RM: reaction microwave, Dr: Drying, Cal: calcination, St: stirring, S: solution, Ref: refluxing.

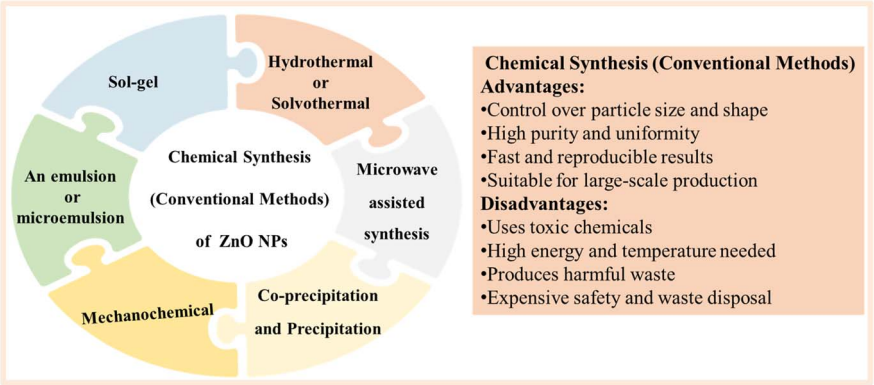

Fig. 2 Key advantages and disadvantages of chemical synthesis methods for the synthesis of ZnO nanoparticles.

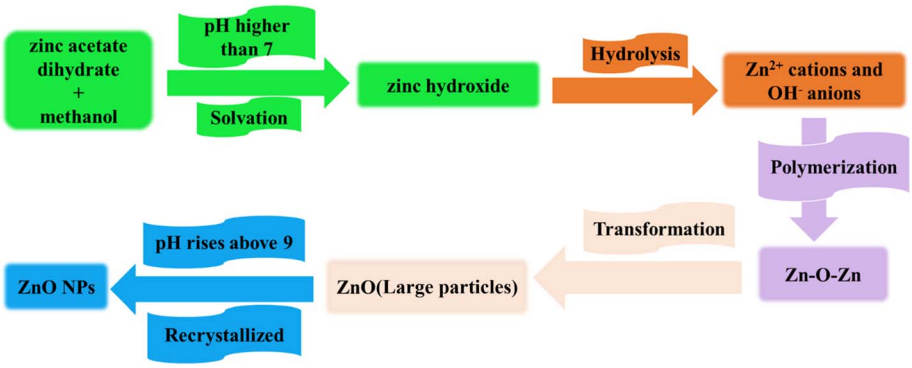

Fig. 3 Sol–gel mechanism for producing ZnO NPs.

ZnO nanoparticle size than XRD, indicating that SEM measures aggregated particles rather than individual crystals.[34]

Behfar *et al.* utilized a sol–gel method at 80 °C to synthesize doped ZnO with copper using $Cu(NO_3)_2$ and $Zn(NO_3)_2$. The characterization of doped ZnO employed many techniques. From UV-Vis data, they calculated band gaps and the following results were obtained: undoped ZnO (3.1 eV), 10% Cu-doped ZnO (2.3 eV), and 25% Cu-doped ZnO (1.8 eV). Additionally, the particle size was determined using XRD spectra, which showed a considerable decrease in the size of ZnO doped with copper (undoped ZnO (180 nm), 10% Cu-doped ZnO (133 nm), and 25% Cu-doped ZnO (40 nm)).[35]

Benamara *et al.* utilized the sol–gel method to prepare indium-doped ZnO NPs at different ratios, 0.01, 0.03, and 0.05, as follows: I0ZO, I1ZO, I3ZO, and I5ZO, using indium chloride, acetate dihydrate, and methanol. The prepared compounds were characterized *via* X-ray diffraction (XRD) analysis, which revealed a wurtzite hexagonal structure with a crystallite size of 65 nm, whereas the sizes of the indium-doped ZnO NPs were I1ZO (53 nm), I3ZO (56 nm), and I5ZO (54 nm). SEM images revealed spherical shapes with agglomeration. The smallest agglomerate was observed for I3ZO. Moreover, EDS analysis exhibited peaks related to oxygen and zinc elements, with a lower concentration of indium. These results agree with the preparation ratios. Additionally, UV-visible showed a slight decrease in band gap energy for indium-doped ZnO NPs (3.19 eV), compared to pure ZnO (3.21 eV), which decreased slightly with rising indium concentration. On the other hand, the authors confirmed the doping process by XPS measurements, which demonstrated distinct core-level spectra for the In 3d, Zn 2p, and O 1 s regions. In the BET analysis, indium-doped ZnO NPs exhibited increased surface area, pore size, and specific surface areas compared to pure ZnO. All the results confirmed an improvement in the performance of indium-doped ZnO NPs.[36]

Shahriiari and Ghorbanpour synthesized Mg-doped ZnO NPs using the sol–gel method. The authors utilized magnesium nitrate, zinc nitrate, and citric acid as chemicals for this study. Characterization techniques included scanning electron microscopy (SEM), which revealed a spherical shape for the Mg-doped ZnO NPs; X-ray diffraction (XRD), which confirmed that the Mg-doped ZnO NPs exhibited a hexagonal wurtzite crystal structure; and UV-Vis spectroscopy, which indicated that the band gap of the Mg-doped ZnO NPs was modified to 3.18 eV, whereas that of pure ZnO was 3.23 eV.[37]

Khamis *et al.* prepared co-doped films of different concentrations using the sol–gel spin coating technique on a glass substrate. The primary objective of this study was to examine the effects of cobalt doping on the structural and optical

characteristics of zinc oxide thin films. The authors investigated the structural and optical properties of zinc oxide thin films. For the assessment of structural properties, X-ray diffraction (XRD) techniques were employed. The results indicated that these films exhibit a hexagonal crystal structure. Additionally, the optical properties were analyzed using a UV-visible spectrophotometer, revealing that absorbance increased with increasing the percentage of dopant (1, 2, 3, and 4 mol%). Furthermore, the energy gap values decreased ranging from 3.32 to 3.03 eV.[38]

2.1.2 Hydrothermal method. In the hydrothermal method, nanoparticles are synthesized by exposing a precursor solution to high temperatures and pressures. Several advantages make this method one of the most popular methods for the synthesis of nanoparticles. Hydrothermal methods make generating nanoparticles of controlled size and shape possible.[39] By carefully controlling parameters such as temperature, pressure, and reaction time, researchers can achieve uniform size distributions and specific shapes of nanoparticles. Furthermore, the hydrothermal method offers a convenient way to produce nanoparticles on a large scale. This technique uses a closed vessel that enhances heat transfer and contains reaction products. As a result, nanoparticle synthesis can be performed with high yields. The hydrothermal approach also promotes green synthesis because water is used as a solvent rather than hazardous organic solvents.[40] Researchers interested in synthesizing nanomaterials find them appealing options because of their simplicity, scalability, and environmental friendliness. Typically, autoclaves are used for this method. A mixture of substrates (white Zn $(OH)_2$ precipitate) was placed inside an autoclave and gradually heated to 100–300 °C, as shown in Fig. 4. Over a certain period, heating continued and cooling followed. Hydrothermal treatment yielded ZnO NPs.

Chen *et al*. successfully prepared pure zinc oxide powder (without organic additives) and zinc oxide powder with additives through hydrothermal processing. The particle morphology, size, organic additives, and reaction temperature were discussed. According to the results, as the reaction temperature increased from 100 to 220 °C, the particle morphology changed from a 1D rod-like shape to a 2D sheet-like shape and then to a 3D crushed stone-like form. The particle size of ZnO powders is influenced by various reaction conditions and the presence of additives. In the absence of additives, particle sizes typically range from approximately 50 to 400 nm, with an increase to 200 to 400 nm observed at elevated temperatures, such as 200 °C. The utilization of templates, such as hexamethylenetetramine and ethylene glycol, results in the formation of smaller particles, ranging from 20 to 100 nm. Conversely, the application of alternative templates can produce significantly larger particles, measuring up to 2 mm. Consequently, it is evident that particle size can be effectively modulated by meticulously adjusting the synthesis parameters and the choice of templates.[39]

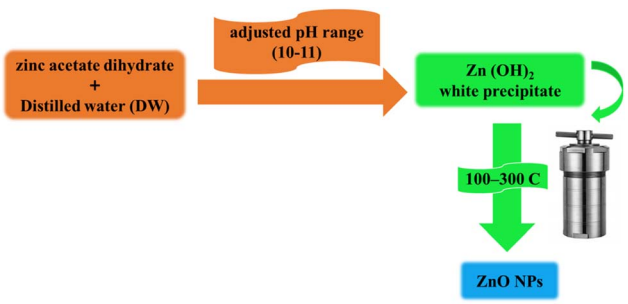

Fig. 4 Graph illustrating the steps involved in the preparation of zinc oxide nanoparticles (ZnO NPs) using the hydrothermal method.

On the other hand, Bulcha *et.al*. synthesized ZnO NPs using hydrothermal processing with sodium hydroxide and zinc nitrate hexahydrate at 300 °C. The characteristics of ZnO NPs by X-ray diffraction (XRD) showed a wurtzite hexagonal structure with an average crystal size of 32 ± 49 nm. Scanning electron microscopy (SEM) was utilized to examine the morphology of the flower-shaped structures. The UV-Vis absorption spectrum showed distinct peaks at 264 nm and 376 nm, corresponding to band gap energies of 4.68 eV and 3.54 eV, respectively.[41]

Basseem *et al.* used a hydrothermal method to prepare pure PZ and co-doped ZnO as Sm La CDZ NPs, La–Sr CDZ NPs, and Sm–Sr CDZ NPs from chemicals zinc acetate dihydrate, samarium nitrate hexahydrate, lanthanum nitrate, and strontium nitrate. XRD analysis revealed a hexagonal crystalline structure and increased average crystallite size for co-doped ZnO NPs. Moreover, UV/Vis spectroscopy showed that the co-doped ZnO revealed a blue shift compared to pure ZnO and the calculated band gap energy increased with co-doped ZnO NP samples. Additionally, SEM and TEM analyses showed a flower-like aggregation of hexagonal nanorods. Additionally, XPS and EDX analyses confirmed the success of the doping process from the significant peaks for Sm^{3+}, La^{3+}, and Sr^{2+} ions. Moreover, the zeta potential of pure and Co-doped ZnO NPs exhibited a positive surface charge.[42]

Zavaleta *et al.* utilized ammonium hydroxide, zinc acetate dihydrate, ethylene glycol, and isopropyl alcohol as solvents for the growth of ZnO nanorods. They prepared two types based on a hydrothermal method: one ZnO NP without ammonium hydroxide and another ZnO NP with ammonium hydroxide. In the characterization of ZnO NPs, optimal control over morphological properties was observed in samples that did not contain ammonium hydroxide. X-ray diffraction (XRD) analysis confirmed the existence of a hexagonal wurtzite crystalline structure, with nanoparticle sizes ranging from 83 to 341 nm. These findings demonstrated consistent results across various synthesis methods, thereby affirming the reproducibility of the results. The estimated band gap values were found to be between 3.45 eV and 3.48 eV, which are marginally higher than that of bulk ZnO (3.37 eV). This variation is attributed to the synthesis conditions, including reaction time and ammonium hydroxide concentration.[43]

Anujency *et al.* employed a hydrothermal method to synthesize doped ZnO nanorods, which advocate for their potential application in commercial photodetector technologies. The doping process involved the incorporation of nickel ions at concentrations ranging from 0% to 5%. The precursors utilized in this synthesis were zinc nitrate and nickel nitrate.

The prepared Ni-doped ZnO nanorods were analyzed *via* various characterization techniques, such as XRD analysis, which confirmed the hexagonal structure. SEM images revealed the formation of homogeneous nanorods. The EDX spectrum displayed prominent peaks corresponding to the elements zinc (Zn), nickel (Ni), and oxygen (O), confirming the efficacy of the doping process. The estimated band gap values for pure ZnO, ZnO:Ni (1%), ZnO:Ni (3%), and ZnO:Ni (5%) samples are roughly 3.20 eV, 3.16 eV, 3.15 eV, and 3.18 eV, respectively, according to optical and UV-Vis spectroscopy measurements. Interestingly, the 3% Ni-doped ZnO displayed the lowest band gap value (3.15 eV) according to the UV-Vis measurements. Furthermore, vibrating sample magnetometry (VSM) analysis of synthesized nanomaterial samples at room temperature demonstrated ferromagnetic characteristics. The samples were evaluated for their performance as photosensors, with the 3% Ni-doped ZnO sample yielding the most favorable results.[44]

Basseem *et al.* synthesized pure, single-doped (La DZNPs, Sm DZNPs, and DZ NPs), and tri-doped ZnO (Sm, La, Sr, T DZ NPs) using a hydrothermal method. The materials used in the synthesis include zinc acetate dihydrate, lanthanum(III) nitrate hexahydrate, samarium(III) nitrate hexahydrate, strontium nitrate, sodium hydroxide (NaOH), and acetic acid. These compounds affect the photodegradation of Reactive Red 43 dye. The Sr DZ NPs recorded the best photodegradation percentage value of 93.43% compared to pure ZnO. After characterization, the authors applied the synthesized nanoparticles as photocatalysts for the degradation of Reactive Red 43. In the characterization step, XRD exhibited a hexagonal crystal structure after doping and showed an increase in the average crystallite size from 25.75 to 30.77 nm; FT-IR showed a shift in the absorption of Zn–O, confirming the doping process for pure ZnO (464.63 cm^{-1}), while doped samples La DZ NPs, Sm DZ NPs, Sr DZ NP, and Sm, La, Sr TDZNPs showed shifted values of 455.14, 512.285, 465.98, and 514.93 cm^{-1}, respectively. UV/Vis spectra recorded an increase in the energy band gap compared with pure ZnO (2.86 eV), but doped samples La DZ NPs, Sm DZ NPs, Sr DZ NP, and Sm, La, Sr TDZNPs showed values of 2.89, 2.93, 2.98, and 3.02 eV, respectively. These results agree with theoretical calculations from DFT, with recorded values of 2.73, 2.77, and 2.85 eV for samples PZ, La DZ NPs, and Sr DZ NPs, respectively. SEM and TEM images exhibited hexagonal and rod shapes that do not change after doping; XPS and EDX confirmed the doping process through the appearance of significant peaks related to doped ions, and pHpzc employed a positive surface charge in all samples.[45]

2.1.3 Microwave-assisted synthesis. Microwave-assisted synthesis has recently garnered significant attention due to its simplicity, reduced reaction time, high yield, and reproducibility. This method operates by converting electromagnetic radiation into thermal energy. Given that various compounds exhibit distinct microwave absorbance characteristics, selective heating takes place within the reaction mixture, leading to the formation of products.[46] The advantages of this method over the hydrothermal method are (a) a shorter reaction time, (b) an inexpensive medium, (c) rapid and selective heating, and (d) controlled morphology of the particles. We produced zinc oxide

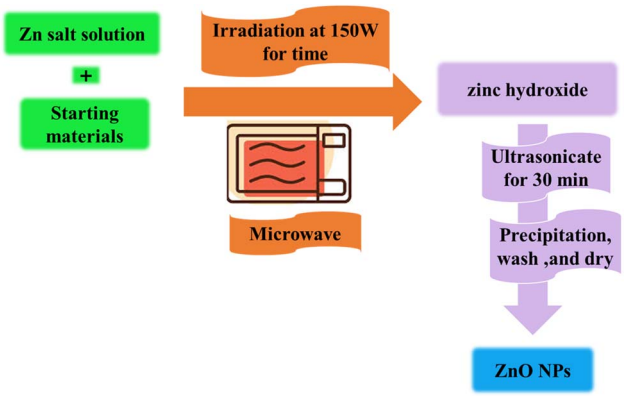

Fig. 5 Microwave-assisted synthesis of zinc oxide nanoparticles.

nanoparticles with various morphologies by combining microwaves with hydrothermal methods.[47,48] A diagram is shown in Fig. 5 illustrating the experimental methodology. In this experiment, zinc hydroxide complexes were synthesized utilizing aqueous solutions of zinc salts and precursor materials, followed by irradiation at 150 W for a specified duration. The resulting complex underwent ultrasonic treatment for 30 minutes. Subsequently, the complex was allowed to rest overnight to facilitate the precipitation of the produced ZnO nanoparticles (NPs).[49]

Verma *et al.* employed a microwave-assisted method alongside a green method to prepare three concentrations of double-doped ZnO using (Fe, Al) in the presence of a green leaf extract from *Murraya Koenigii*. The three concentrations involved changed the concentration of Al (0.001 M), whereas the concentration of ZnO (nearly 0.046 M) and Fe (0.001 M) remained nearly the same. XRD analysis of the double-doped ZnO revealed crystallite sizes ranging from 17 to 31 nm, which varied with the concentration of the Al dopant. SEM and TEM images displayed spherical shapes with an average particle size of approximately 20.56 nm. UV-Vis results indicated improved electronic and optical properties, with the bandgap decreasing from 2.99 to 2.88 eV.[50]

Nandhini *et al.* prepared zinc oxide nanoparticles using both microwave radiation and natural reductants extracted from *Ocimum americanum* and *Euphorbia hirta*. The optimal conditions for synthesis included a zinc sulfate concentration of 12.8 mM, 12 min of irradiation, and a 26 : 1 ratio of plant extract. Characterization using UV-Vis spectroscopy revealed a peak at 292 nm, indicating the successful conversion of zinc sulfate to zinc oxide. Scanning electron microscopy (SEM) images showed that the nanoparticles had a cuboid shape and an average size of 70.37 ± 7.8 nm. Fourier-transform infrared spectroscopy (FTIR) confirmed the presence of various functional groups associated with the components of *E. hirta* and *O. americanum* extracts, verifying their role as reducing agents in the preparation of ZnO nanoparticles. X-ray diffraction (XRD) analysis indicated that the nanoparticles consisted of 24.1% crystalline and 75.9% amorphous phases. The zeta potential of the nanoparticles was measured to be 20 mV.[51]

Rustembekkyzy *et al.* employed a microwave-assisted method to synthesize various ZnO nanoparticles in a single step, using different molar concentrations of zinc acetate dihydrate (0.035-ZnO, 0.07-ZnO, 0.14-ZnO, 0.28-ZnO, and 0.56-ZnO). These nanoparticles were utilized in photocatalytic activity studies to degrade methylene blue (MB) under solar light illumination. The authors used SEM and TEM imaging techniques to investigate the morphological structures of ZnO, which revealed a transition from rod-like to sheet-like forms as the concentration of the Zn precursor increased. Analysis of the synthesized nanoparticles indicated a hexagonal phase of zinc oxide, with XRD data used to calculate the crystallite size in the range of 22.4–48.4 nm. The computed energy band gap, derived from UV-Vis spectra data, was found to be between 2.84 and 2.98 eV. A sample with a sheet-like structure, specifically 0.56 M–ZnO, exhibited the highest photocatalysis percentage of 96.6%.[52]

Porrawatkul *et al.* employed a reducing agent extracted from *Averrhoa carambola* fruit and microwave assistance to synthesize pure and Ag-doped ZnO nanoparticles for coating cotton fabrics. Different concentrations (0.05, 0.07, 0.10, and 0.15 mol L^{-1}) of silver nitrate hexahydrate were used to prepare the treated fabrics at various pH values. FT-IR spectroscopy confirmed the successful preparation of ZnO and the incorporation of silver into ZnO. The XRD data revealed the crystalline nature of ZnO nanoparticles, whereas the Ag/ZnO nanoparticles exhibited a face-centered cubic structure. Additionally, SEM images displayed spherical nanoparticles. In the presence of Ag, the surface morphology of ZnO consisted of smaller, spherical nanoparticles compared to those of undoped ZnO. The particle size distribution ranged from 20 to 30 nm, which is smaller than that of the synthesized Ag nanoparticles (30–70 nm). EDX data further confirmed the successful green synthesis of Ag-doped ZnO nanoparticles. SEM images of the untreated fabrics displayed a clean and smooth surface, while the treated fabrics revealed some natural patterns. The elemental compositions of Zn, O, and Ag in the treated cotton were determined through EDX analysis.[53]

2.1.4 Precipitation method or co-precipitation method. The precipitation method is an established, controlled, and reproducible procedure employed in the large-scale production of powdered nanoparticles with predictable characteristics for industrial applications.[49] The process is divided into two stages: (a) the precipitation of a ZnO precursor from solution and (b) the thermal treatment of this precursor, followed by milling to induce physical disintegration of the calcined agglomerates and removal of contaminants.[27,54] A capping agent is utilized in this process to prevent nanoparticle agglomeration. Temperature and calcination strategies can influence the production of ZnO nanoparticles. ZnO nanoparticles were effectively synthesized using a direct precipitation approach, which involved a zinc salt and a precipitation agent. The reactants were agitated to create a precipitate, which was then filtered and rinsed with distilled water. Finally, thermal treatment was applied, as shown in Fig. 6.

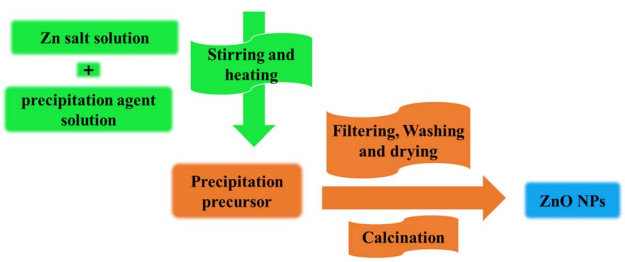

Fig. 6 Precipitation method of ZnO NPs.

Kumar *et al.* synthesized flower-like zinc oxide nanostructures using a precipitation method. These nanoparticles were primarily created with a metal precursor (zinc acetate dihydrate) and a precipitating agent (sodium hydroxide). This study involved the analysis of synthesized ZnO utilizing techniques such as SEM and TEM. The results revealed the formation of crystalline ZnO structures resembling flowers, characterized by clusters of ZnO nanorods arranged in a leaf-like configuration, followed by the emergence of ZnO nanostructures with a floral morphology. XRD confirmed the formation of hexagonal ZnO nanostructures of the space group $P6_3mc$, CPDS Card No. 03-65-3411).[55]

Ghaznavi *et al.* synthesized copper-doped and undoped ZnO NPs using the chemical co-precipitation method as new anticancer agents against G-292 (bone cancer) and MRC-5 (normal lung fibroblast) cells after 24 and 72 h of exposure. X-ray diffraction analysis of all synthesized nanoparticles revealed a wurtzite crystal structure for both Cu-doped and undoped ZnO NPs, while SEM analysis showed a spherical morphology for undoped ZnO NPs with an average size of 15–39 nm. In contrast, Cu-doped zinc oxide nanoparticles exhibited both rod-like and grain-like structures, with a relatively large average grain size of 18–68 nm. Additionally, TEM analysis displayed a spherical shape with an increased size for the Cu-doped zinc oxide nanoparticles. Furthermore, zeta potential measurements indicated a negative zeta potential for all synthesized nanoparticles.[56]

Truong *et al.* synthesized zinc oxide nanoparticles (ZnO NPs) using the chemical precipitation method, employing zinc acetate dihydrate and sodium hydroxide as precursors. They produced two types of ZnO NPs: one capped with poly(*N*-vinylpyrrolidone) (PVP) and the other without PVP. Characterization *via* X-ray diffraction (XRD) showed that both types of ZnO NPs matched the hexagonal wurtzite structure (JCPDS 00-001-1136). Using Debye–Scherrer's formula, the calculated crystallite sizes were 24.6 nm for ZnONPs-PVP and 26.1 nm for ZnO NPs without PVP. Additionally, UV-Vis spectroscopy revealed significant absorption peaks in the 360–370 nm range, indicating the formation of ZnO NPs, which were also used to determine the energy band gaps *via* Tauc's method. The energy band gap was found to be 3.4 eV for ZnONPs without PVP and 3.3 eV for ZnONPs-PVP. Furthermore, TEM images showed that both types exhibited a hexagonal shape; however, the PVP-capped ZnONPs displayed some shadowing effects.[57]

DIN *et al.* illustrated the synthesis of cobalt-doped zinc oxide nanoparticles (ZnO NPs) using a co-precipitation method involving zinc nitrate hexahydrate, cobalt nitrate hexahydrate,

ammonium hydroxide, and hexadecyltrimethylammonium bromide (CTAB) as precursors. Characterization of both undoped and doped ZnO NPs confirmed their successful preparation through UV-visible spectroscopy, which showed an absorption band at 654 nm. Additionally, FT-IR spectroscopy revealed a peak at 1164 cm^{-1}, indicating the presence of doped cobalt in the ZnO lattice. SEM analysis demonstrated that the doped ZnO NPs exhibited a spherical shape with a porous structure and vacancies at their centers.[58]

In the study by Rezaei *et al.* zinc sulfate heptahydrate and sodium hydroxide were used as precursors for the precipitation of ZnO NPs. The synthesized nanoparticles were analyzed by XRD after the calcination process. The results indicated an increase in crystallite size, as determined by Scherrer's equation, with an average diameter of 80–90 nm for the pyramidal rod morphology and 800–900 nm for the star-like morphology. Additionally, SEM analysis revealed that the morphology and size of the synthesized ZnO particles are highly sensitive to temperature, resulting in the formation of sphere-like, pyramidal, pyramidal-rod, rod-like, star-like, and plate-like morphologies. Furthermore, zeta potential (ZP) measurements showed values of 33.2 mV for the pyramidal rod morphology and 11.8 mV for the star-like morphology.[59]

2.1.5 Solvothermal method. Solvothermal synthesis is a solution-based process that produces ZnO nanoparticles in a sealed autoclave under high pressure and temperature. This method employs organic solvents as the reaction medium instead of water, making it comparable to the hydrothermal approach. An organic solvent, such as ethanol, methanol, ethylene glycol, or dimethyl formamide (DMF), is used to dissolve a zinc precursor, such as zinc acetate, zinc nitrate, or zinc chloride. A base, typically NaOH or KOH, is then added to initiate the precipitation process. Following this, the solution was heated for several hours at temperatures ranging from 100 to 250 °C in a Teflon-lined autoclave, as illustrated in Fig. 7.[60] The high-temperature and high-pressure environment promotes the formation of structured ZnO nanostructures.[60] In some preparations, a surfactant is mixed with the zinc salt while stirring for 20 minutes. The closed chamber is then placed in a heated source to maintain the necessary temperature. Finally, the precipitate was collected, washed several times with ethanol and water, and dried at room temperature in air.

The solvothermal method presents several advantages, particularly when organic solvents are utilized for the synthesis of zinc oxide (ZnO) nanoparticles. One significant benefit is the increase in precursor solubility in organic solvents, facilitating the production of ZnO nanoparticles with uniform size, well-defined morphology, and high crystallinity. Furthermore, organic solvents can reduce particle agglomeration and improve dispersibility by functioning as stabilizing agents. The characteristics of the nanoparticles, including surface chemistry and aspect ratio, can be tailored by varying reaction parameters such as temperature, pressure, and the type of solvent employed. This method also allows for the incorporation of dopants and the formation of composite materials, thereby broadening the functional applications of ZnO nanostructures. Overall, solvothermal synthesis remains a robust technique for the generation of high-quality metal oxide nanoparticles, owing to its inherent versatility, reproducibility, and scalability.[61,62]

As previously reported, Ravbar *et al.* synthesized ZnO NPs using a simple one-pot solvothermal method, followed by microwave-assisted grafting of transition metals onto the surface of the NPs, starting from zinc acetate dihydrate and nickel chloride precursors. Characterization was conducted using various techniques. X-ray diffraction patterns demonstrated that ZnO retains its wurtzite hexagonal structure, and slight changes in the lattice parameters suggest surface attachment rather than lattice substitution. Adsorption–desorption isotherms indicated that nickel decoration increased the specific surface area from 37 $m^2 g^{-1}$ to 39 $m^2 g^{-1}$, although this difference was not statistically significant. The UV/Vis spectrum of Ni-modified ZnO shows a slight blue shift at the absorption edge, which is correlated with a significant increase in band gap energy, thereby enhancing the photocatalytic activity of Ni-modified ZnO. TEM and XRD studies

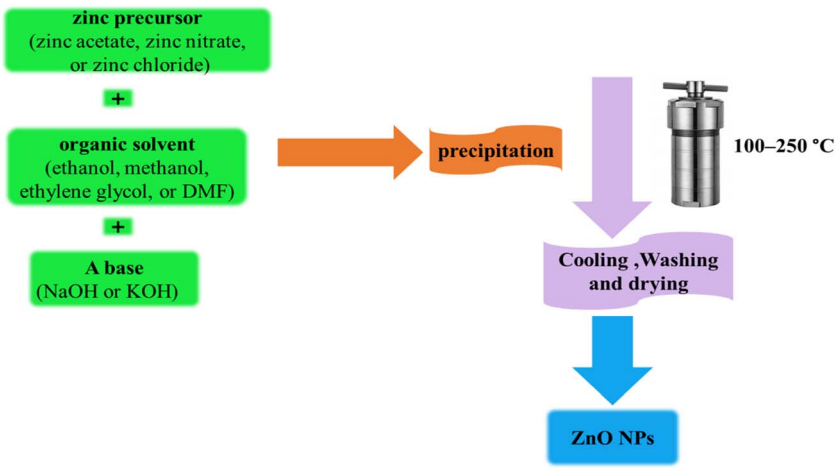

Fig. 7 Schematic diagram outlining the sequential steps involved in the solvothermal method used to synthesize ZnO nanoparticles (NPs).

indicate that bare ZnO nanoparticles have an average size of ~13 nm, while Ni addition (0.5 wt%) does not appreciably alter this size. Increasing microwave power leads to larger particles (~22 nm) and longer structures (80–150 nm). XRD reveals that the size changes are mostly related to synthesis conditions, not Ni inclusion. XPS analysis revealed the presence of Ni^{2+} species, which do not significantly integrate into the zinc oxide lattice parameters, thus indicating successful surface grafting. Furthermore, zeta potential measurements demonstrated that the nickel-decorated samples exhibited a more negative surface charge than the non-decorated samples, which facilitated improved adsorption of pollutants.[63]

Prayoga *et al.* investigated the generation, characterization, and sensing efficacy of zinc oxide (ZnO) nanoflowers as active materials for ethanol detection. The ZnO nanoflowers were synthesized utilizing a solvothermal technique, with glycerol serving as a capping agent and 2-propanol as a solvent. XRD analysis confirmed the formation of highly crystalline wurtzite-phase ZnO, while SEM provided morphological insights, revealing that the ZnO nanoflowers comprised of one- and two-dimensional nanostructures arranged into a three-dimensional hierarchical architecture. The synthesized ZnO demonstrated optimal sensing performance as an ethanol sensor.[64]

Segovia *et al.* reported that the solvothermal treatment of nanometric zinc oxide as a zinc ion source enables the production of three distinct types of one-dimensional zinc oxide nanostructures. This method involves an agglomeration/melting mechanism that produces large nanoneedles. When stearic acid is present, a similar process yields nanorods. The significantly reduced aspect ratio (d/l) observed with this addition appears to result from a lower pH in the medium and the probable interaction of the carboxylic acid with the [0001] crystal plane surface. ZnO nanowires are also formed by using the layered hybrid nanocomposite ZnO/stearic acid as a zinc source under the same reaction conditions as those used for the ZnO-fatty acid mixture. In this case, the development mechanism of one-dimensional nanostructures seems to involve a rolling-up/surfactant-segregation process rather than typical ZnO crystallite growth. By varying the precursor and reaction times, they were able to create morphologically uniform phases corresponding to ZnO nanoneedles, nanorods, or nanowires. Compared with bulk zinc oxide, the photocatalytic activities of the prepared nanostructures in degrading methylene blue were comparable.[65]

Muhammad *et al.* employed an absolute ethanol-based solvent and reducing agent to fabricate Cu_2O/TiO_2 and Cu_2O/ZnO (CZ) heterojunction photocatalysts using a one-pot solvothermal technique. The two heterojunction nanocomposites are cuprous oxide/titanium dioxide (CT) and cuprous oxide/zinc oxide (CZ). Characterization *via* studying XRD patterns revealed that Cu_2O exists in its cubic phase, while TiO_2 and ZnO exist in their respective crystalline states. Pure Cu_2O had a computed average crystallite size of 11.190 nm. The CT (1.5–1.5) and CZ (1.5–1.5) nanocomposites had average crystallite diameters of 22.890 nm and 29.240 nm, respectively. TEM analysis showed that Cu_2O nanoparticles, measuring approximately 5–7 nm, were uniformly and securely dispersed on irregular ZnO and TiO_2 particles. Electron diffraction revealed clear lattice stripes corresponding to the component materials, confirming the formation of p–n heterojunctions. UV-vis absorption spectra indicated that Cu_2O, TiO_2, and ZnO absorb a broad range of wavelengths from 220 to 800 nm, effectively utilizing visible light.[66]

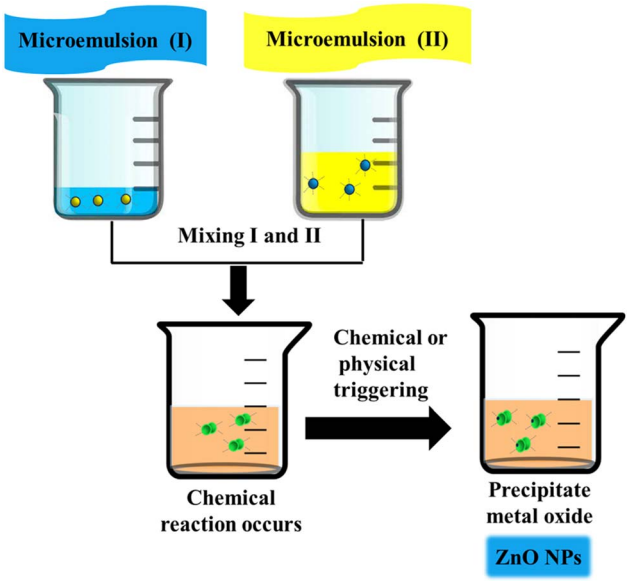

Fig. 8 Schematic representation of ZnO nanoparticle synthesis using emulsion or microemulsion techniques.

2.1.6 Emulsion or microemulsion synthesis. Emulsions are defined as continuous liquid phases that are dispersed by a second discontinuous, immiscible liquid phase, as depicted in Fig. 8. Depending on the characteristics of the external phase, emulsions can be classified into two primary types: oil-in-water emulsions and water-in-oil emulsions. In this context, "water" is understood to refer to any highly polar, hydrophilic liquid, whereas "oil" signifies hydrophobic, nonpolar liquids.[23] A liquid solution formulated in this manner exhibits thermodynamic stability and optical isotropy. In the present study, zinc oxide nanoparticles were synthesized utilizing reverse microemulsion.[67]

Yıldırım and Durucan synthesized ZnO nanoparticles employing a modified reverse microemulsion process, systematically examining the influence of calcination temperature and surfactant concentration on particle size and morphology. Their findings indicated that the utilization of a low surfactant concentration (5 : 5: 90) produced spherical ZnO nanoparticles with an average size of approximately 15 ± 1 nm; this size increased to approximately 24 ± 1 nm at elevated calcination temperatures. Conversely, a higher surfactant concentration (30 : 5 : 65 ratio) resulted in the formation of rod-like structures at calcination temperatures of 300 °C and 400 °C, resulting in lengths of 66–72 nm and diameters of 22 ± 3 and 28 ± 1 nm. At a calcination temperature of 500 °C, the particles transitioned back to a spherical morphology, a change attributed to defect accumulation and thermodynamic stabilization. The increase in the calcination temperature was associated with enhanced green emission at 530 nm, indicative of oxygen vacancies and

zinc interstitials. SEM and TEM images confirmed the morphological alterations resulting from the variety of synthesis conditions.[68]

Gholami *et al.* developed an innovative pH-responsive nanocarrier composed of polyethylene glycol (PEG), polyvinyl alcohol (PVA), and zinc oxide nanoparticles (ZnO NPs) characterized by a substantial surface area. The synthesis of a nanocarrier encapsulating quercetin (QC) was achieved through a water/oil/water (W/O/W) emulsification method. Subsequent characterization was conducted utilizing X-ray diffraction (XRD) and Fourier-transform infrared spectroscopy (FT-IR). The nanocarriers were further analyzed using scanning electron microscopy (SEM), dynamic light scattering (DLS), and zeta potential measurements to assess particle size, surface charge, and stability. The incorporation of ZnO NPs significantly enhanced the loading and encapsulation efficiencies of QC. Drug release studies demonstrated controlled and pH-sensitive release profiles at pH values of 5.4 and 7.4. Comparative analyses of PEG/PVA/ZnO nanocomposites against the PEG/PVA and control groups revealed a marked reduction in cell viability upon treatment with the PEG/PVA/ZnO nanocomposites.[69]

To synthesize copper-zinc mixed oxides, Pawlonka *et al.* employed a microemulsion technique that utilized a water-in-oil (W/O) microemulsion. The continuous oil phase consisted of cyclohexane, while the dispersed phases included aqueous solutions of copper nitrate and zinc nitrate. Hexadecyltrimethylammonium bromide (CTAB) served as the surfactant, and isopropanol functioned as a co-surfactant. The authors explored various synthesis phase sequences, including co-precipitation within a microemulsion, reduction with hydrazine, and subsequent calcination at 350 °C. Additionally, sodium carbonate was utilized as the precipitating agent. The CuO–ZnO-1 sample was obtained by co-precipitation in the microemulsion, whereas the CuO–ZnO-2 sample was obtained by reducing copper with hydrazine before mixing with microemulsions containing zinc and carbonate ions. Under these conditions, CuO–ZnO-4 was prepared with twice the amount of surfactant. After applying hydrazine to a microemulsion containing $Zn(NO_3)_2$ and Na_2CO_3, a CuO–ZnO-3 sample was formed. Furthermore, from XRD it was observed that the CuO–ZnO-2 sample has the smallest CuO and ZnO particles. With increasing surfactant concentration, the ZnO size changes from 13.9 to 35.4 nm. This is more noticeable in copper oxide crystallites, whose size increases from 11.4 to 20.1 nm. Temperature-programmed reduction (TPR) was conducted to evaluate redox characteristics; it was found that an increase in surfactant concentration during synthesis led to a decrease in the reducibility of CuO. The most significant reduction in reducibility was observed for the CuO–ZnO-3 sample. BET was utilized to assess the surface area and porosity. With a specific surface area of 27.3 $m^2 g^{-1}$, CuO–ZnO-1 had the highest specific surface area. In the SEM images, the CuO–ZnO-4 samples differ morphologically from the remaining samples. In the presence of a smaller amount of surfactant, sponge-like morphologies are observed.[70]

Cuenca *et al.* developed a bicontinuous microemulsion method using sodium dodecyl sulfate (SDS), sodium bis2-ethylhexyl sulfosuccinate (AOT), $Zn(NO_3)_2$, NaOH, and toluene to synthesize high-purity ZnO NPs. Varying the $Zn(NO_3)_2$ concentration, NaOH feeding time (100–150 min), and surfactant/toluene ratio (50/50–60/40) affected particle size and distribution. The 60/40 ratio confirmed bicontinuous structure (high conductivity), yielding ~98% pure, highly crystalline hexagonal ZnO. Particle size decreased (≈21.7 to 6.0 nm) with increasing $Zn(NO_3)_2$ content, and TEM showed particles of 3–9 nm.[71]

Lim *et al.* synthesized aluminum-doped ZnO (AZO) nanorods *via* a microemulsion method by mixing surfactants such as sodium benzene sulfonate (SBS) and dodecyl benzene sulfonic acid sodium salt (DBS) with zinc acetate in xylene, followed by the addition of an aluminum nitrate precursor and reflux heating. The samples synthesized with the two surfactants were AZO-SBS, AZO-DBS, ZnO-SBS, and ZnO-DBS. XRD confirmed a hexagonal wurtzite structure, with slight lattice shrinkage in AZO due to the smaller Al^{3+} ion. SEM showed uniform rod-like structures (~80 nm diameter, several microns long). PL spectra displayed strong emission at 383 nm; the two different surfactants were measured at 2.8×10^3, 3.3×10^3, 7.0×10^6, and 3.3×10^7 Ωcm for the samples AZO-SBS, AZO-DBS, ZnO-SBS, and ZnO-DBS, respectively. These results indicate that Al-doped ZnO exhibits lower resistivity compared to undoped ZnO, confirming successful doping into the ZnO lattice.[72]

2.1.7 Mechanochemical process. Mechanochemical or solid-state reactions represent a suitable method for manufacturing nanoparticles on a large scale due to their inherent simplicity and low cost.[73] The advantages of this method include that it does not utilize organic solvents. However, a significant limitation of this method is the prolonged reaction time, which can extend from several hours to several weeks.[74] The process typically involves dry milling at low temperatures, where precursor materials are subjected to high-energy ball-powder impacts, thereby initiating the desired chemical reactions. Moreover, during this reaction, the precursor materials are often diluted with a diluent, commonly sodium chloride (NaCl), as illustrated in Fig. 9. After milling, the powder mixture underwent calcination, followed by the

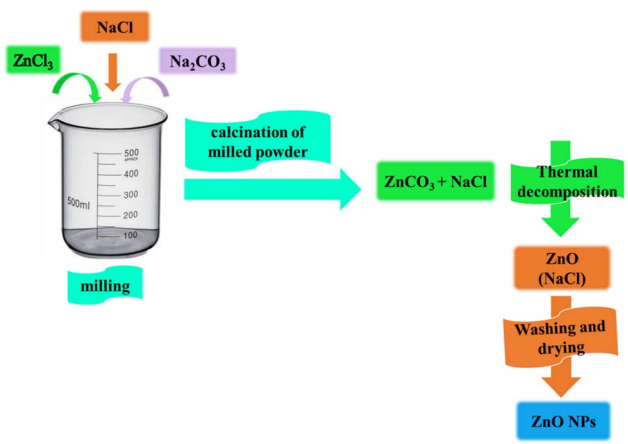

Fig. 9 Mechanochemical synthesis of ZnO NPs.

thermal decomposition of zinc carbonate ($ZnCO_3$). The diluent acts as a reaction medium, facilitating the separation of nanoparticles and inhibiting their growth, thereby effectively reducing the risk of significant agglomeration.

Stanković *et al.* synthesized ZnO nano-powders using mechanochemical processing with thermal treatment. Initially, the reaction mixture of oxalic acid and zinc chloride was milled for 0.5h-4hs before being subject to thermal treatment at 450 °C for 1 hour. This study examined how milling duration, and the presence of oxalic acid affected the morphology, crystallite size, average particle size, and overall structure of the ZnO nanopowders. XRD and Raman spectroscopy were employed to characterize the samples. The XRD analysis of the prepared ZnO revealed a well-defined long-range order and a pure wurtzite structure in the synthesized ZnO powders; however, Raman spectroscopy indicated a different middle-range order. Additionally, the Raman spectra showed that the lattice defects and impurities introduced into the ZnO crystal structure depend on the milling duration, regardless of the thermal treatment applied. Laser diffraction was used to assess particle size distribution, while scanning electron microscopy (SEM) was used to determine the powder morphology. Inductively coupled plasma analysis was used to investigate impurity contamination. The results indicated that the two-step technique employed is effective for producing highly crystalline ZnO nanopowders, which are characterized by uniformly spherical particles with diameters ranging from 20 to 50 nm. This study illustrates the significant role of an aqueous oxalic acid solution in preventing agglomeration of the final product.[75]

Dumitrescu *et al.* prepared a ZnO/hydroxyapatite nanocomposite by combining zinc oxide (ZnO) with hydroxyapatite (HA) at various mass ratios. The nanopowders were prepared using ethanol and subjected to ball milling for 0.5 hours at a speed of 400 rpm, followed by drying at 0 °C. The photocatalytic degradation of methyl orange (MO) as a synthetic dye was assessed under stirring conditions and UV (ultraviolet) irradiation. The photodegradation percentages demonstrated that the most effective removal of MO from aqueous solutions *via* photodegradation was achieved with the samples CZH3 (containing 75% ZnO) and CZH_4 (containing 25% ZnO), both exhibiting similar photocatalytic activity. Conversely, sample CHZ_2 (composed of 100% HA) demonstrated minimal photocatalytic degradation. The high absorbance of the suggested nanocomposites indicates their potential application as photocatalysts in wastewater treatment, facilitating the retention of organic contaminants. The ability of the composite nanopowders to retain MO dye was evaluated using XRD, whereas differential scanning calorimetry and thermogravimetric analysis were employed to assess the MO dye retention capacity. These findings indicate that the produced composites can be used as cutting-edge materials to cleanse wastewater and prevent dye-type organic contaminants.[76]

Nazir *et al.* described a mechanochemical method for synthesizing polypyrrole/Ag–ZnO (Ppy/Ag–ZnO) heterostructures. The synthesized catalyst was characterized using XRD, which confirmed the hexagonal wurtzite structure corresponding to JCPDS file No. 36-1451. A crystallite size of 2.30 nm was calculated using Debye–Scherrer's equation for the Ppy/Ag–ZnO nanocomposite. GA showed that the thermal stability of Ppy/Ag–ZnO is greater than that of pure Ppy. FT-IR showed a peak at 596 cm^{-1}, which is attributed to the presence of Ag-doped ZnO, whereas SEM images showed aggregated particles with an average diameter of 2.65 μm. The BET surface area was 47.08 cm^3 g^{-1}, and zeta potential measurements showed a negative charge of the nanocomposite.[77]

Zinc oxide (ZnO) nanoparticles were synthesized by Otis *et al.*, using a solvent-free mechanochemical process that involved high-energy ball milling of ε-$Zn(OH)_2$ crystals at a 1 : 100 powder-to-ball mass ratio under ambient conditions. During milling, crystalline ε-$Zn(OH)_2$ was transformed into amorphous $Zn(OH)_2$, which then decomposed into ZnO and water. Various characterization techniques have been employed, including X-ray Diffraction (XRD), which revealed both crystalline and amorphous phases in the powders. It produced uniform ZnO nanoparticles with sizes of 10–30 nm, based on the milling duration. TEM data displayed small spherical nanoparticles, while DLS indicated a uniform size distribution of approximately 500 nm. UV-Vis spectroscopy, using Tauc plots, was utilized to determine the band gap of the ZnO nanopowders, which was found to be 3.22 eV. The TGA analysis data identified three main steps in the decomposition process. The photocatalytic activity of the synthesized nanoparticles was evaluated using methyl orange (MO) dye, and the authors demonstrated that photocatalytic efficiency increased with the number of milling cycles due to increased concentration of ZnO.[78]

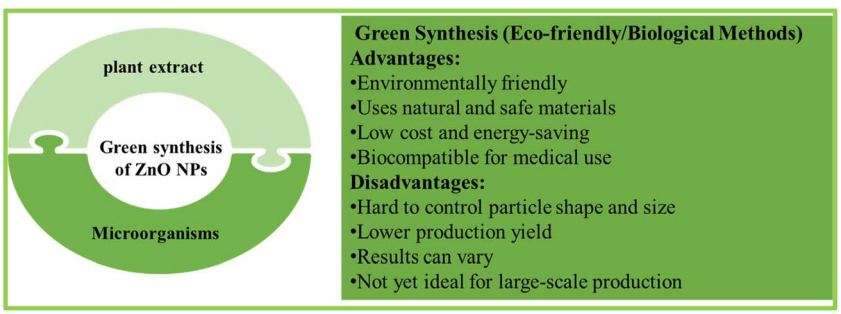

Fig. 10 Key advantages and disadvantages of green methods for the synthesis of ZnO nanoparticles.

Table 2 Green synthesis of ZnO nanoparticles using biological sources, including precursors, synthesis conditions, properties, and applications[a]

No.	Bio source	Precursors	Synthesis conditions	Properties	Applications	Ref.
1	Plant	Avocado, papaya, and mango fruits, and zinc nitrate hexahydrate	RE: heated 30 min with a magnetic stirrer RS: stirred for 1 h and left to settle for 24 h at normal temperature	The average crystallite sizes and shapes were: avocado (11 ± 20 nm) was rod-like, mango (16 ± 30 nm) was flower-like, papaya (21 ± 10 nm) was nanotube-like	Antimicrobial	86
2	Plant	Azadirachta indica (Meliaceae) (neem) and zinc nitrate hexahydrate	RE: heated for 20 min at 60 °C RS: boiled at 60–80 °C and heated in a furnace at 400 °C for 2 h	Average crystallite size 18 nm with a spherical shape	Antimicrobial activity	136
3	Plant	Beta vulgaris, cinnamomum tamala, cinnamomum verum, Brassica oleracea var. Italica, and zinc nitrate	RE: boiled for 15 min. RS: boiled at 60–70 °C and heated in a furnace at 400 °C for 2 h	*Beta vulgaris*: spherical, ∼20 ± 2 nm *Cinnamomum tamala*: Rod-shaped, ∼30 ± 3 nm *Punica granatum*: spherical-like, agglomerated, ∼46 ± 2 nm Brassica oleracea var. italica: spherical, cluster-like, ∼47 ± 2 nm	Antibacterial and antifungal activity	137
4	Plant	Sida rhombifolia linn and zinc nitrate hexahydrate	RE: boiled at 60–80 °C. RS: heated in furnace at 300 °C for 2 h	ZnO-NP agglomeration with an average size of ∼30 nm	Genotoxic study and antibacterial activity	138
5	Plant	Camellia Sinensis var. Assamica with zinc acetate and sodium hydroxide	RE: boiled at 85 °C for 30 minutes. RS: heated in an oven at 200 °C for 5 h	Average crystallite size: 18–60 nm with a sponge-like asymmetrical shape	Antibacterial activity	139
6	Plant	Aqueous fruit extracts of myristica fragrans and zinc acetate dihydrate	RE: heated at 150 °C for 20 min, powdered in an incubator at 37 °C overnight RS : Calcined for 2 h at 500 °C	Crystallite size: 41.23 nm with a spherical shape	Biological and photocatalytic	140
7	Plant	Mangosteen (*Garcinia mangostana* L.) leaf and zinc nitrate hexahydrate	RE: heated at 70–80 °C for 20 min RS: calcined at 400 °C for 2h in a muffle furnace	Average particle size: 14.21 nm, with a spherical shape	Antibacterial	141
8	Plant	Leaves of *Ocimum sanctum* L. and zinc nitrate hexahydrate	RE: boiled for 30 min RS: dried at 300 °C for 4 h; similar procedure followed at the other two temperatures (400 °C and 500 °C)	300 °C: spherical, clumped; avg. Size 36 nm (XRD 18 nm) 400 °C: spherical, hexagonal, uniform, average size 30 nm (XRD 12 nm) 500 °C: spherical, more segregated, average size 31 nm (XRD 17 nm)	Antibacterial activity	142
9	Microorganism	*Enterobacte Cloacae* and zinc acetate	MO: isolated from the formation water of an oil field (southwest of Iran). RS: Incubated for 24 h, kept in an oven for 6 h at 400 °C	Average crystallite size from 32 to 58 nm with amorphous form	Enhanced oil recovery (EOR)	143

Table 2 (*Contd.*)

No.	Bio source	Precursors	Synthesis conditions	Properties	Applications	Ref.
10	Microorganism	*Bacillus megaterium and Zinc nitrate*	MO : Bacteria from Oxoid, UK for cultivated use, nutrient and chocolate blood agar, RS : Incubated at 37 °C for 48h	Average crystallite size 45 – 95 nm with rod-like and cubic shapes	Antimicrobial	144
11	Microorganism	*Lactobacillussporogens* and zinc chloride solution	MO: from lactic acid Bacillus spore tablets. RS: incubated for 9 hours	Average crystallite size: 5–15 nm with hexagonal, tubular and other irregular forms	Controlling pollutant	145
12	Microorganism	*Sphingobacterium thalpophilum,* and zinc nitrate solution	MO: fresh bacterial strain S. thalpophilum (KM019199.1). RS: annealed at 700 C for 5 h	XRD (Scherrer equation): average size ∼37 nm, ESEM: triangular chip-like structures, average size ∼112 nm	Antimicrobial	146
13	Microorganism	*Aspergillusterreus* and $ZnSO_4$	MO: fungus from the Institute of Microbial Technology, microbial type culture Collection and Gene Bank, Chandigarh, India. RS: incubated at 150 rpm at 32 °C for 2 days	Average crystallite size: 54.8∼82.6 nm with a spherical shape	Antifungal	147
14	Microorganism	*Streptomyces* sp. and zinc chloride	MO: isolated from marine soil collected from the Kodiyakkarai marine segment of Tamilnadu, India RS : Incubated at 30 °C for 72 h at 220 rpm	Average crystallite size: 20–50 nm with a spherical shape	Anticancer and antibacterial activity	148
15	Microorganism	Bacillus licheniformis MTCC 9555 and zinc acetate dihydrate	MO: from the Department of microbiology, College of life sciences, Gwalior, India. RS: incubated for 48 h	Average crystallite size: 250 nm with a flower shape	Photocatalytic activity	149
16	Microorganism	*Aspergillus fumigatus* TFR-8 (NCBI GenBank accession no. JQ675291) and zinc nitrate	MO: isolated from the central agricultural research farm (26 180 N 73 010 E) of the Central arid zone research Institute (CAZRI), Jodhpur, India	Average crystallite size: 1.2∼6.8 nm with oblate, spherical, and hexagonal shapes	Agriculture	16

[a] Note: reaction for extraction: RE, reaction of synthesis: RS, microorganism: MO.

2.2 Green synthesis for the synthesis of ZnO NPs (eco-friendly/biological methods)

An efficient and environmentally sustainable method for synthesizing nanoparticles is the green method, which uses natural, non-toxic, and renewable resources such as plants and microorganisms. This method operates at mild temperatures and pressures, minimizing or eliminating the use of hazardous chemicals and solvents, as illustrated in Fig. 10. The biosynthesis of nanoparticles involves using microorganisms and plants for synthesis, as detailed in Table 2. This approach is environmentally friendly, safe, cost-effective, green, and biocompatible.[93] Green synthesis is defined as a process that avoids toxic and dangerous chemicals.[94] As green methods have gained popularity, various studies have been conducted to synthesize ZnO NPs from diverse sources, including bacteria, algae, fungi, plants, *etc*. A biomimetic approach facilitates the large-scale production of ZnO nanoparticles free from additional impurities, demonstrating higher catalytic activity while limiting the use of toxic chemicals. Moreover, it is important to note that while this review highlights and compares the reported green synthesis procedures, detailed mechanistic differences, including the specific roles of phytochemicals or microbial metabolites and their influence on nanoparticle formation, are not systematically discussed in most of the referenced studies.

2.2.1 Green synthesis of ZnO NPs using plant extracts. Owing to their high content of phytochemicals, plant parts, including leaves, stems, roots, fruits, and seeds, have been used for centuries, which facilitate the synthesis of ZnO NPs. Notably, the presence of antioxidants in plants, such as amino acids, vitamins, polysaccharides, alkaloids, polyphenols, saponins, flavonoids, and terpenoids, exhibits reductive properties. Consequently, plant extracts can work as reducing and capping agents in zinc salt solutions, thereby enabling the formation of ZnO NPs. Through bio-reduction, phytochemicals can effectively reduce metal ions and metal oxides to zero-valence metal NPs. Moreover, natural extracts derived from plant materials are environmentally friendly, cost-effective, and do not necessitate the use of intermediate base groups. This method is characterized by its efficiency, minimal time requirements, lack of expensive equipment or precursors, and the production of a pure product that is enriched in quantity and free from contaminants. Consequently, it represents a widely employed approach for the synthesis of ZnO NPs from plant sources.[95]

The simple extraction process begins with the careful washing of the plant material in running tap water, followed by rinsing with double-distilled water. The plant parts are then air-dried at room temperature, weighed, and crushed into small pieces. Milli-Q H_2O is added to the ground plant parts at the desired concentration, and the resulting mixture undergoes thermal treatment while being stirred continuously with a magnetic stirrer and subsequently filtered. Following filtration, a clear solution is obtained, which is designated the plant extract (sample), as illustrated in Fig. 11. Additionally, the obtained extract is mixed with a certain volume of zinc salt, then the mixture is heated to the desired temperature and maintained for a specific duration to ensure effective mixing. Finally, the mixture is washed and dried to yield crystalline nanoparticles.[96]

Sana Zahoor *et al*. used the leaf extract of *Senecio chrysanthemoides* which included flavonoids, alkaloids, polyphenolic derivatives, and other macromolecules. These substances are believed to be physiologically active, acting as reducing agents that facilitate the conversion of zinc ions (Zn^{2+}) into zinc oxide nanoparticles (ZnO NPs) and using zinc acetate-2-hydrate in the synthesis of ZnO NPs. ZnO nanoparticles are formed through a biomolecule-mediated reduction process, where polyphenols and flavonoids reduce Zn^{2+} ions. Moreover, proteins and functional groups present in the extract act as natural capping and stabilizing agents, controlling nucleation, growth, and particle morphology. Subsequent thermal treatment removes organic residues and enhances crystallinity. The reduction process and

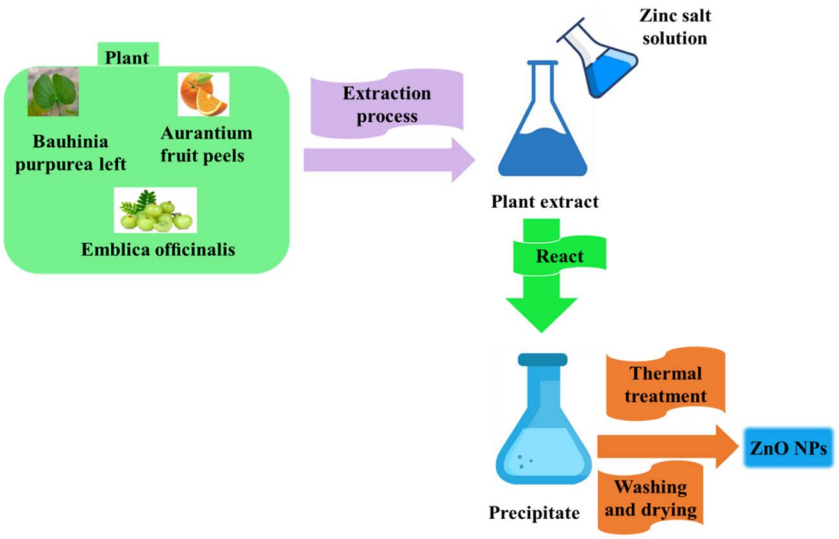

Fig. 11 Schematic diagram representing synthesized ZnO NPs using plant extract as a green synthesis method.

stability of the nanoparticles can be influenced by the pH of the reaction mixture, which may alter the charge of both the zinc ions and biomolecules. ZnO NPs have demonstrated high stability within the pH range of 3 to 11. Employing a UV-Vis spectrophotometer, they identified a distinct absorption peak at 349 nm that confirms the formation of ZnO NPs. Moreover, FT-IR showed a strong band obtained at 349 cm^{-1}, indicating the presence of ZnO NPs in the mixture. Based on SEM analysis, the ZnO NPs exhibited a morphology resembling crushed ice, characterized by a uniform particle size, whereas the elemental composition was elucidated through energy-dispersive X-ray spectroscopy (EDX). Additionally, XRD analysis confirmed that the ZnO NPs had an average particle size of 31 nm and showed hexagonal wurtzite crystallinity.[97]

Kocabas and Dogan prepared ZnO NPs using a biosynthetic method that involved treating zinc acetate with *Veronica multifida* leaf extract. The primary metabolites in plant biological systems include alkaloids, terpenoids, polyphenols, and carbohydrates. These substances are essential for converting metal ions into nanoparticles (NPs). In the described study, the green synthesis of ZnO NPs was specifically conducted using leaf extract from *Veronica multifida*. These findings indicate that the production process is facilitated by the active compounds present in *Veronica multifida* leaves. They characterized the biosynthesized ZnO NPs using UV-Vis (ultraviolet-visible) spectroscopy, which showed absorption peaks at 240 nm for pH 7 and 360 nm for pH 12. X-ray diffraction (XRD) revealed a more intense peak at pH 12 compared to pH 7. FT-IR exhibited stronger bands at pH 12 at 480, 709, 1034, and 1088 cm^{-1} than at pH 7. Additionally, transmission electron microscopy (TEM) confirmed that the size of the ZnO NPs ranged from 10 to 100 nm.[98]

Abomuti *et al.* prepared biosynthesized ZnO nanoparticles utilizing phytochemicals derived from an aqueous leaf extract of *S. officinalis* in conjunction with a zinc nitrate solution. The leaves are rich in various phytochemicals that function as stabilizing and reducing agents during nanoparticle synthesis. In this process, Zn^{2+} ions are reduced to ZnO nuclei by phenolic compounds and flavonoids, which additionally act as capping agents to stabilize and regulate the formation of the nanoparticles. The concentration of the zinc nitrate solution (*e.g.*, 0.2 M), temperature (*e.g.*, 50 °C), stirring duration (*e.g.*, 2 hours for the first reaction and 2 hours for precipitation), and pH adjustment (*e.g.*, maintaining pH 12) are crucial factors in the synthesis of ZnO NPs. Together, these elements influence ZnO NP nucleation, stability, and electrostatic interactions between Zn^{2+} and biomolecules.

The characterization of the biosynthesized ZnO NPs was conducted through multiple analytical techniques. Ultraviolet-visible (UV-Vis) spectroscopy revealed an absorption peak at 368 nm, with the bandgap calculated *via* the Tauc plot to be 2.96 eV. Additionally, the application of Scherrer's equation, derived from X-ray diffraction (XRD) analysis, indicates that the average crystallite size is 11.89 nm. Scanning electron microscopy (SEM) revealed a rough, irregular material with little accumulation, while EDX showed high-intensity peaks for zinc metal, oxygen, and carbon, likely associated with biological molecules. Transmission electron microscopy (TEM) demonstrated an average particle size of 26.14 nm ± 2.46 nm for the biosynthesized ZnO NPs. Moreover, FT-IR confirmed the characteristic spectral features of the aqueous leaf extract of *S. officinalis*. Photoluminescence spectra further validated the potential of *S. officinalis* extract as both a reducing and stabilizing agent. BET surface area analysis indicated a surface area of 53.001 $m^2\ g^{-1}$, a pore volume of 0.240 cc g^{-1}, and a pore diameter of 3.052 nm. Thermogravimetric/differential scanning calorimetry analysis (TGA/DTG) revealed three different stages of significant weight loss without any weight loss occurring above 780 °C.[99]

Alharbi *et al.* prepared ZnO NPs using a phytochemical method, utilizing *A. absinthium* leaves. The main active phytochemicals involved in the production of ZnO NPs include polyphenols and flavonoids. These substances are rich in hydroxyl and carbonyl groups and serve as effective capping and reducing agents that influence the size and dispersion of nanoparticles. Tannins are phenolic compounds that can strongly adhere to ZnO nuclei, regulating growth and preventing aggregation. Saponins may affect surface charge and stability due to their surfactant properties. Although the role of alkaloids is less defined, they may contribute to stabilization and reduction. These authors employed several techniques to analyze the biosynthesized ZnO NPs in comparison to those synthesized without the extract. FTIR results showed an absorption band for green ZnO NPs at 432.05 cm^{-1}, while ZnO without extract exhibited a band at 439.77 cm^{-1}. UV-Vis spectroscopy was employed to determine the band gap of green ZnO and ZnO nanoparticles (without extract), yielding values of 2.65 eV and 2.79 eV, respectively.

Furthermore, SEM analysis showed spherical shapes, while XRD analysis revealed a hexagonal structure with an average particle size that decreased from 24.39 to 18.77 nm. EDX analysis showed three significant peaks at energies of 1 keV, 8.7 keV, and 9.8 keV corresponding to zinc, and a peak at 0.5 keV related to oxygen, all of which are characteristic of ZnO nanoparticles. BET analysis provided values for pore volume and average pore diameter, with BET surface areas of 4.003 $m^2\ g^{-1}$ for ZnO without extract and 6.032 $m^2\ g^{-1}$ for green ZnO NPs, while the pore volumes were 0.011 $cm^3\ g^{-1}$ for ZnO without extract and 0.017 $cm^3\ g^{-1}$ for green ZnO NPs.[100]

Fouda *et al.* utilized the peel aqueous extract of *Punica granatum* to biosynthesize ZnO NPs. The aqueous peel extract of *Punica granatum* served as the active component in this study for synthesizing ZnO nanoparticles. Various bioactive metabolites in the peel extract, including polyphenols such as flavonoids, tannins, anthocyanidins, and phenolic acids, reduce zinc acetate to form ZnO nanoparticles. The characterization of the biosynthesized ZnO NPs was conducted using UV-Vis spectroscopy, which revealed an absorption peak in the range of 350–380 nm, indicative of ZnO NPs. FT-IR analysis identified various functional groups referring to compounds present in the plant extract, suggesting their role in the reduction of ZnO NPs. X-ray diffraction (XRD) analysis demonstrated the absence of numerous peaks in the diffraction pattern, indicating high purity, and the crystallite size was calculated to be 43 nm. TEM

exhibited an average particle size of 25.1 nm, which ranged from 10 to 45 nm for the biosynthesized ZnO NPs. SEM images showed that the particles had spherical shapes.[101]

2.2.2 Green synthesis of ZnO NPs using microorganisms. Microorganisms play a crucial role as nano-factories for the accumulation and detoxification of heavy metals. This process primarily involves various reductase enzymes that convert metal salts into metal nanoparticles. Research has shown that different microorganisms, including bacteria, fungi, and algae, can produce nanoparticles both inside and outside their cells. These microbes are capable of synthesizing organic materials within their cells and transporting them externally.[102] Microorganisms, including bacteria, fungi, and algae, can synthesize zinc oxide (ZnO) nanoparticles *via* biological mechanisms. This process primarily involves the reduction of zinc ions to ZnO, a reaction facilitated by enzymes and biomolecules synthesized by microorganisms, which also act as natural capping and stabilizing agents. The synthesis of ZnO nanoparticles occurs *via* two predominant pathways: extracellularly and intracellularly. In extracellular synthesis, proteins and metabolites produced outside the microbial cells reduce the concentration of zinc ions in the surrounding environment. Conversely, intracellular synthesis transpires within the microbial cells, where zinc ions are bio-reduced and subsequently accumulate as nanoparticles.[103] Eco-friendly synthesis methods are advantageous because they avoid the use of toxic chemicals; however, they may yield lower yields and pose challenges for separation from biofilms.

Furthermore, the use of microbes for the environmentally sustainable production of metal nanoparticles offers several benefits, including a rapid, cost-effective, clean, non-toxic, and environmentally friendly approach to generating nanoparticles with diverse sizes, shapes, compositions, and physicochemical properties.[104,105] The main disadvantages of microorganism-based metal nanoparticle production include challenging steps such as microbiological sampling, isolation, culture, and storage. Additionally, recovering the nanoparticles produced through this method requires downstream processing. Microorganisms can synthesize NPs *via* the enzymatic reduction of metal ions in their environment, effectively trapping them to form elemental forms. Enzymes, proteins, and other microbial components play significant roles in the reduction process[106] (Fig. 12).

Barsainya and Singh *et al.* utilized *P. aeruginosa*, a microorganism known for producing the siderophore pyoverdine in response to zinc ion stress, to synthesize zinc oxide (ZnO) nanoparticles through the bio-reduction of zinc nitrate. In this process, pyoverdine interacts with zinc ions (Zn^{2+}) *via* functional groups such as hydroxamate, amino, and carboxyl moieties. This interaction facilitates the reduction and transformation of zinc ions into ZnO nanoparticles at ambient temperature, eliminating the need for external chemical reducing agents. The effectiveness of the green synthesis mediated by pyoverdine was confirmed through various characterization techniques, which demonstrated that the biosynthesized ZnO nanoparticles exhibited a polycrystalline wurtzite phase, with predominantly spherical morphology, a size range of 50–100 nm, stabilization through hydroxamate and amino groups, and an absorption peak at 416 nm.[107]

Iqtedar *et al.* utilized a *B. cereus* strain to synthesize ZnO NPs from eighteen bacterial isolates, with eight demonstrating confirmed synthesis of ZnO NPs. The primary mechanism for producing these nanoparticles is extracellular enzymatic reduction. In this process, bacteria release NADPH-dependent reductase enzymes into the culture medium, facilitating the conversion of NADPH to $NADP^{+}$. The electrons generated during this reaction are captured by zinc ions at the cell surface, leading to their reduction and the formation of elemental zinc oxide nanoparticles. The authors characterized ZnO NPs using UV-Vis, FTIR, XRD, and SEM techniques. The ZnO NPs exhibited a sharp peak at 352 nm and had a band gap of 3.5 eV. FT-IR spectra confirmed that the stabilizing agents are related to carbohydrates and amines by determining the characteristic bands related to specific functional groups. SEM images exhibited irregular rod shapes, whereas a zeta sizer indicated a size range of 58.77–63.3 nm. Moreover, the zeta potential was measured at −7.39 mV.[108]

Yusof *et al.* investigated the biosynthesis of ZnO NPs utilizing the zinc-tolerant probiotic *Lactobacillus plantarum* TA4, derived from both the cell-free supernatant (CFS) and cell biomass (CB). The proposed biosynthesis mechanism involves the participation of enzymes, proteins, and other organic compounds present in

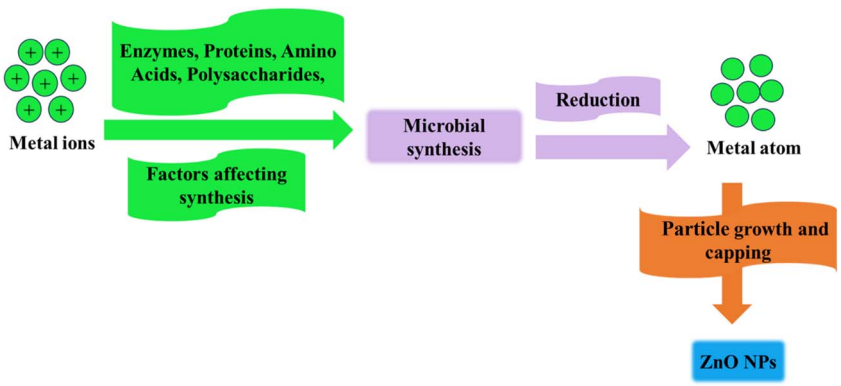

Fig. 12 Schematic diagram representing the green synthesis of ZnO nanoparticles using microorganisms.

the CFS and CB, which function as reducing agents for Zn^{2+} ions. These ions are subsequently converted into ZnO nanoparticles through the action of functional groups on the bacterial cell surface and associated proteins. The characterization of the biosynthesized ZnO NPs derived from CFS and CB was confirmed through various analytical techniques. UV-Vis spectroscopy revealed absorption peaks at 349 nm for ZnO NPs-CFS and at 351 nm for ZnO NPs-CB, indicating the successful synthesis of the ZnO NPs. FT-IR analysis showed the presence of carboxyl, hydroxyl, and amide functional groups associated with both types of biosynthesized ZnO NPs. These findings suggest that the biosynthesis process of ZnO involves reducing and stabilizing agents. DLS measurements showed dispersity indices of less than 0.4 for both ZnO NPs-CFS and ZnO NPs-CB, reflecting their stability in suspension. Additionally, TEM imaging revealed that ZnO NPs-CFS exhibited a flower-like morphology with a particle size of 291.1 nm, whereas ZnO NPs-CB displayed an irregular shape with a particle size of 191.8 nm[109].

Devendra *et al.* demonstrated the biosynthesis of ZnO NPs utilizing the zinc-tolerant bacterium *Serratia nematodiphila*. These bacteria employ unidentified enzymes to facilitate the reduction of zinc ions (Zn^{2+}) to elemental zinc (Zn). This initial reduction process is essential for the nucleation and subsequent formation of ZnO nanoparticles. Following the formation of zinc atoms, the residual Zn^{2+} ions are further reduced to their oxide form (ZnO). Additionally, the authors confirmed the synthesis of ZnO NPs using UV-vis spectroscopy, which showed a surface plasmon resonance (SPR) absorption peak at 379 nm. XRD analysis indicated high purity and a crystallite size of 24.79 nm corresponding to the (101) peak. These results agree well with the TEM results, which revealed similar size ranges of 15 to 30 nm, with an average diameter of 23.09 ± 4.23 nm and shapes that were roughly spherical. The DLS results indicated uniform sizes ranging from 10 to 30 nm, supporting the TEM findings, whereas the zeta potential was recorded at −33.4 mV, confirming the stability of the biosynthesized ZnO NPs. Finally, the authors utilized these compounds to investigate their antifungal and antimicrobial properties, as well as their effectiveness in the photodegradation of methyl orange.[110]

Abdullah *et al.* utilized the bacterial strain *P. aeruginosa* (NMJ15) isolated from mangrove sediment samples to synthesize zinc oxide nanoparticles (ZnO-NPs) through a green biosynthesis approach. This environmentally friendly synthesis process is predicated on the bacterial metabolites present in the cell-free filtrate (CFF), which function as reducing and stabilizing agents. Functional groups such as carbonyl (C═O), hydroxyl (O–H), amine (NH), and thiol (SH) groups facilitate the reduction of zinc ions from zinc acetate dihydrate to form ZnO nanoparticles, initially yielding a white precipitate. This precipitate underwent calcination at 150 °C to yield crystalline nanoscale ZnO. The synthesis procedure commences with inoculating the bacterial strain into nutrient broth, followed by incubation, centrifugation, washing, and a subsequent incubation to isolate the CFF. The addition of zinc acetate to the CFF at a pH of 8.5 induces the formation of hydrated ZnO, which is thereafter converted into stable nanoparticles. The formation of ZnO-NPs was confirmed through various characterization

Table 3 Comparison of conventional and green ZnO nanoparticle synthesis methods in terms of particle-size control, environmental toxicity, cost, and scalability

Method	Particle-size control	Environmental toxicity	Cost	Scalability	Ref.
Sol–gel	Excellent control (narrow distribution, tunable morphology)	Moderate to high (alcohol solvents, metal alkoxides)	Moderate (requires controlled hydrolysis, heating)	High (widely used in industry)	150 and 151
Hydrothermal	Very high; pressure and temperature provide precise tuning	Low-moderate (water is the main solvent)	Moderate–high (due to autoclave equipment)	High (batch and continuous reactors available)	150 and 152
Precipitation	Moderate (affected by pH and mixing)	Moderate (uses NaOH, metal salts)	Low	Excellent (easiest for industrial production)	153
Solvothermal	High	Moderate to high (organic solvents)	Moderate	Moderate (depending on reactor volume)	154
Emulsion	High (micelle size controls ZnO NP size)	Moderate (surfactants, hydrocarbons)	High (due to surfactants)	Moderate	155
Mechanochemical	Moderate	Low (no solvents)	Very low	Excellent (industry-friendly)	156
Green synthesis (plant extracts)	Medium	Low to moderate (depends on phytochemicals)	Very low	Very low (waste plant extracts)	157 and 158
Green synthesis (microbial – bacteria, fungi, algae)	Moderate	Extremely low	Very low	Low to moderate (depending on culture systems)	159 and 160

techniques: UV-Vis spectroscopy demonstrated a surface plasmon resonance (SPR) absorption peak at 380 nm, indicating successful nanoparticle synthesis; transmission electron microscopy (TEM) images revealed spherical nanoparticles with dimensions ranging from 6 to 21 nm, which was consistent with XRD analysis confirming a crystalline structure with an average particle size of 21 nm by using the Debye–Scherrer equation. FT-IR analysis further identified the involvement of O–H, C═O, NH, and SH (thiol) functional groups in the bacterial metabolites, which play a crucial role in reducing and stabilizing the nanoparticles.[111]

Finally, an evaluation of various synthesis routes of ZnO-NPs was conducted, focusing on critical factors, such as particle size control, environmental toxicity, cost, and scalability (Table 3). Traditional chemical methods enable precise control over particle size and morphology through techniques such as sol–gel, hydrothermal, solvothermal, precipitation, and microemulsion processes. However, these traditional methods often rely on hazardous chemicals, organic solvents, and high-energy conditions, which result in increased toxicity and higher production costs. In contrast, green synthesis methods that employ natural reducing and stabilizing agents, such as plant extracts, bacteria, or fungi, offer an environmentally sustainable alternative. This methodology significantly reduces chemical waste and mitigates environmental hazards; nevertheless, it is limited by challenges related to reproducibility, variability in extracts, and inadequate control over particle size distribution.

3 Applications of ZnO NPs

Zinc oxide nanoparticles (ZnO NPs) have attracted considerable scholarly interest owing to their distinctive physicochemical properties, which encompass a high surface area, a broad band gap, tunable morphology, and multifunctional reactivity. These attributes enable their utilization across diverse domains, including environmental remediation, optoelectronics, ultraviolet protection, biomedical applications, industrial applications, and agriculture.

3.1 Environmental (photocatalysis)

ZnO NPs are excellent photocatalytic materials under both UV and visible light, which allows them to efficiently degrade organic pollutants, dyes, and pharmaceutical contaminants in water. In addition to their high surface reactivity, they can generate reactive oxygen species (ROS), which makes them ideal for the purification of water and self-cleaning of surfaces.

Benamara *et al.* utilized indium-doped ZnO NPs to test the photodegradation activity of Rhodamine B dye, and recorded the best photodegradation percentage under visible light irradiation of 93% for 3% indium-doped ZnO.[36] Moreover, the degradation of RR43 dye showed that the Sm–Sr CDZ NPs had the best photodegradation percentage value of 91.31%, and the degradation process followed the pseudo-first-order kinetics model. A recyclability test employed degradation of RR43 dye under UV irradiation more than once and confirmed the stability of the prepared nanoparticles.[42] Double-doped ZnO (Fe, Al) nanoparticle samples were utilized in water purification to remove Rhodamine dye, achieving a photodegradation percentage value of 97%.[50] The nanoparticles modified with cobalt were tested for methylene blue (MB) degradation. A recyclability test conducted over four cycles demonstrated the stability of the synthesized Co-doped ZnO nanoparticles. The highest degradation rate for these nanoparticles was recorded at a reaction time of 14 min ($K_{app} = 0.053\ min^{-1}$). This outcome can be attributed to the increased band gap and surface area resulting from the doping process.[58] The nanoparticles were applied in two key areas of application. First, in the photocatalytic process, these nanoparticles nearly doubled the efficiency of reducing hexavalent chromium (Cr(VI)) to the less toxic trivalent form (Cr(III)) when the nickel content was 0.5 wt%. However, when microwave power was used during the synthesis of ZnO, structural elongation occurred, resulting in a reduction in performance. Second, the materials exhibited strong performance in an immobilized photoreactor, effectively degrading five pharmaceutical contaminants. Notably, the addition of nickel significantly increased naproxen removal from 65% to 75%.[80]

Heterojunction photocatalysts of Cu_2O/TiO_2 and Cu_2O/ZnO (CZ) were tested under visible illumination to assess their photocatalytic activity, with the CZ (1.5–1.5) nanocomposite achieving rapid and complete dye degradation. Enhanced charge separation at the heterojunction interfaces contributed to high efficiency by minimizing recombination and promoting the formation of reactive radicals, which facilitated dye decomposition. BET surface area measurements confirmed that the photocatalysts exhibited excellent adsorption capabilities. Due to their combined structural, optical, and surface properties, these materials demonstrate outstanding photocatalytic performance, providing an effective and rapid method for dye removal from the environment.[66] Researchers utilized an aqueous extract of Punica granatum peel for the biosynthesis of ZnO NPs. They tested the biosynthesized ZnO NPs for catalytic activity toward methylene blue dye. The highest degradation percentage of methylene blue dye, achieved using UV-light irradiation, was 93.4 ± 0.2% under conditions of 20 g mL^{-1} after 210 minutes of exposure to UV light.[101]

The exceptional photocatalytic activity of the ZnO@HAp nanocomposite underscores its significant potential for environmental remediation. The material's remarkable ability to remove organic dyes from aqueous solutions was evidenced by a rapid degradation efficiency of 96.6% for methylene blue within a mere 30 minutes. Furthermore, 62% of the widely utilized antibiotic ciprofloxacin was degraded within the same timeframe, demonstrating the composite's effectiveness in the removal of pharmaceutical contaminants. ZnO@HAp exhibited a notable capacity for reducing chemical oxygen demand (COD) in wastewater treatment applications, with household sludge experiencing an 88% reduction after 150 min of irradiation, indicating its efficacy in decomposing complex organic materials. The pH of the solution was found to significantly influence the photocatalytic degradation behavior of pollutants when utilizing ZnO@HAp. Experimental results indicated that the maximum degradation efficiency (96.4%) was achieved in 30

minutes at a neutral pH of 7. The observed decline in performance under acidic conditions (pH < 7) was attributed to the partial solubility of ZnO, which may lead to catalyst dissolution and reduced activity. Conversely, at alkaline pH values (pH > 7), lower adsorption and degradation efficiency were noted, as the catalyst surface becomes more negatively charged, thereby weakening the electrostatic interactions with positively charged dye molecules. These findings illustrate that a neutral pH environment enhances electrostatic interactions and catalytic efficiency, rendering it optimal for the degradation of methylene blue. Therefore, precise pH regulation is essential for wastewater treatment systems to achieve optimal photocatalytic activity and efficient pollutant removal. After five consecutive cycles of reuse, the material exhibited over 87% efficiency, indicating exceptional stability and favorable reusability. The significantly higher specific surface area of the ZnO@HAp composite (110.124 $m^2 g^{-1}$) compared to pure ZnO (30.2 $m^2 g^{-1}$) contributes substantially to its enhanced photocatalytic performance, providing increased adsorption capacity and active sites for photocatalytic processes.[112]

The examination of the potential of zinc oxide (ZnO) nanostructures for photodegradation highlights the critical influence of particle size on photocatalytic efficiency. Two distinct morphologies were synthesized: ZnO nanoparticles (ZnO NPs) exhibiting a crystallite size of approximately 35 nm, and ZnO quantum dots (ZnO QDs) with a size of approximately 7.5 nm. Both nanostructures were utilized as photocatalysts under UV-Vis irradiation to decompose organic dyes, including fluorescein, methylene blue (MB), and Rhodamine 6G (Rh6G). UV-Vis spectral analysis, which monitored the degradation process, revealed a significant reduction in the characteristic absorbance peaks of each dye with prolonged irradiation time. After 60 min of UV irradiation at a catalyst concentration of 100 μg mL^{-1}, ZnO QDs demonstrated superior photocatalytic activity, achieving degradation rates of up to 92.64% for MB and 53.62% for Rh6G, as determined by quantitative analysis. Conversely, ZnO NPs achieved degradation rates of 44.95% for Rh6G and approximately 61.32% for fluorescein under identical conditions. The enhanced photocatalytic efficacy of ZnO QDs can be ascribed primarily to their reduced size, which increases the surface area-to-volume ratio, thereby increasing the number of active sites available for dye adsorption and facilitating more effective charge transfer. Kinetic analyses employing the Langmuir–Hinshelwood model indicated that the degradation of the dyes followed *pseudo*-first-order kinetics, with significantly higher rate constants (k) for the ZnO QDs, indicating accelerated degradation rates.[113]

Through effective dye removal under UV/visible irradiation, the biosynthesized ZnO and C-doped ZnO photocatalysts demonstrate considerable potential for wastewater treatment applications. The carbon-doping process significantly enhances photocatalytic activity, as evidenced by the degradation of crystal violet (CV) and methyl orange (MO), which serve as model cationic and anionic dyes, respectively. At an initial dye concentration of 10 mg L^{-1}, the most effective catalyst—5% C-doped ZnO calcined at 500 °C—achieved degradation rates of 92.7% for CV and 87.8% for MO within 200 minutes. The incorporation of carbon reduced the optical band gap from 3.09 eV (for pure ZnO) to 2.93 eV, thereby enhancing the charge-separation efficiency and increasing visible-light absorption. With a carbon concentration of 5%, the photocatalytic activity followed pseudo-first-order kinetics, with rate constants increasing from 0.00438 to 0.00746 min^{-1} for CV and from 0.00554 to 0.00998 min^{-1} for MO. The correlation coefficients ($R^2 = 0.99$) confirmed the adequacy of the kinetic fitting model. Furthermore, operational parameters significantly influenced degradation efficiency: at a catalyst dose of 75 mg, complete removal (100%) of both dyes was achieved; however, when the initial dye concentration was increased to 50 mg L^{-1}, the degradation efficiency decreased to 68.84% for CV and 29.67% for MO. pH levels also proved critical; acidic conditions promoted MO removal through electrostatic interactions, whereas alkaline conditions facilitated CV degradation.[114]

Overall, ZnO-based photocatalysts exhibit significant efficacy in degrading dyes, pharmaceuticals, and hazardous compounds when exposed to both UV and visible light, particularly when optimized *via* methods such as doping, heterojunction formation, or size reduction. Despite their consistently high degradation efficiencies, the photocatalytic performance of these materials is markedly affected by various operational parameters, including pH, catalyst loading, and pollutant concentration. Furthermore, the instability of ZnO under acidic conditions, along with the predominance of laboratory-scale studies using model contaminants, imposes significant limitations on its practical application.

3.2 Optoelectronics

Zinc oxide nanoparticles (ZnO NPs) are extensively utilized in optoelectronic devices due to their significant band gap of approximately 3.37 eV and their robust exciton binding energy of approximately 60 meV. Their applications encompass gas sensors, photodetectors, light-emitting diodes (LEDs), and ultraviolet (UV) light emitters. The high electron mobility and chemical sensitivity of ZnO NPs render them particularly suitable for integration into photonic and electrical devices. A piezoelectric system developed by depositing a ZnO nanoparticle film on the surface of a steel beam utilized a 20 MHz DDS function generator and a Fotonic MTI-2100 sensor to measure the displacement of the beam in response to square wave voltages ranging from 1 to 10 V at frequencies of 1 Hz and 50 Hz. The displacements observed due to the ZnO nanoparticle film confirm its piezoelectric behavior. The consistent displacement under constant voltage further demonstrates the stability and functionality of the ZnO film.[43]

Furthermore, ZnO NPs produced from *Cordyline fruticosa* extract exhibited optoelectronic characteristics, making them suitable for use in electron transport layers. The ZnO NP films demonstrate variable transmittance and absorbance depending on their thickness. For instance, a layer with a thickness of 4175.95 nm exhibited the lowest optical transmittance but the highest absorbance, peaking at 1.40 at 346.4 nm. The study investigated five different film thicknesses: 883.43 nm, 2450.50 nm, 3715.25 nm, 4175.95 nm, and 4625.35 nm. The energy band gap was calculated using the Tauc plot equation.

Electrically, the ZnO·NPs demonstrated enhanced conductivity. This enhancement reduces electron–hole recombination by increasing electron mobility and injecting photoexcited electrons into the conduction band. The electrical behavior was evaluated using a four-point probe device. X-ray diffraction (XRD) analysis revealed a hexagonal wurtzite crystalline structure for ZnO·NPs, with distinct peaks at 2θ values of 32°, 34°, 36°, 47°, 56°, 63°, and 68°. The nanoparticles exhibited good crystallinity, as indicated by narrow and strong diffraction peaks, and were free of undesirable contaminants. Using the Debye–Scherrer formula, the average crystallite size was determined to be 25 nm based on the peak at 36°, which corresponds to the (101) plane. Furthermore, SEM images revealed a crystalline form with a hexagonal structure and TEM analysis estimated the nanoparticle size to be between 25 and 52 nm, confirming their nanoscale dimensions.[115] The produced zinc oxide films show great promise for a range of optical applications. The large band gaps of these materials, which range from 3.14 eV to 3.9 eV, make them suitable for use in optical devices. Additionally, the materials exhibit a significant absorbance peak at 350 nm, indicating UV sensitivity, which makes them ideal for UV detectors. The strong UV absorbance and high visible reflectance (up to 90%) of these films suggest potential for energy conversion in transparent structures, such as solar cells integrated into windows. Overall, their optical characteristics, particularly their high transmittance and low absorption of visible light, indicate their suitability for various optoelectronic applications.[116]

Zinc oxide (ZnO) nanoparticles (NPs) and doped ZnO NPs exhibit optoelectronic properties, making them useful for various applications, including photovoltaic systems. Higher concentrations of doped Sn led to an increase in the optical band gap of ZnO NPs. Pure ZnO has a band gap of 3.55 eV. As the Sn doping increases, the band gap shifts: 1% Sn-doped ZnO NPs had a band gap of 3.72 eV, 3% showed 3.74 eV, 5% showed 3.79 eV, 7% showed 3.81 eV, and 10% had 3.85 eV. The Burstein-Moss shift, where Sn^{4+} ions replace Zn^{2+} ions or occupy unoccupied sites, causes an increase in carrier concentration and a decrease in carrier mobility. All Sn-doped ZnO NP thin films demonstrate high transparency in the visible range, which rapidly decreases in the UV region. Pure ZnO thin films have an average optical transmittance of approximately 87%, with an absorption edge at approximately 369 nm. While 1 wt% doped films exhibit lower transmittance than pure films due to increased optical scattering from rougher surfaces, the 10 wt% Sn-doped ZnO thin film shows the highest transparency among the doped samples, with an average transmittance of 98.65%. Both pure and Sn-doped ZnO thin films display n-type semiconductor characteristics. The bulk carrier concentration in pure ZnO thin films is 2.46×10^{11} cm^{-3}. This concentration increases significantly with Sn doping, reaching 3.03×10^{13} cm^{-3} at 10% Sn doping. This increase is attributed to Sn^{4+} ions replacing Zn^{2+} ions or occupying unoccupied sites, resulting in additional free electrons. However, mobility tends to decrease as the Sn doping concentration increases. The resistivity of thin films decreases from 1.46×10^{4} Ω cm for pure ZnO to a minimum of 9.60×10^{2} Ω cm with 5% Sn doping, after which it increases with increasing doping level.[117]

This research demonstrated that optoelectronic switching memory systems based on ZnO nanoparticle-embedded polymer matrices exhibit highly concentration-dependent electrical performance. When ZnO nanoparticles were loaded beyond a threshold mass concentration (Rm) of approximately 0.05 wt%, conductance increased significantly, by about three orders of magnitude. ZnO nanoparticles formed inhomogeneous percolative conducting channels connecting the top and bottom electrodes, leading to a substantial increase in conductivity above Rm = 0.03 wt%. A suitable concentration window of approximately 0.05–2 wt% ZnO was identified for reliable memory operation through systematic optimization; devices with 0.05–0.1 wt% ZnO nanoparticles displayed consistent and repeatable resistive switching over multiple cycles. Notably, the highest ON/OFF resistance ratio was achieved near $R_m = 0.03$ wt%. During a positive voltage sweep (0–1 V), the devices exhibited repeatable bipolar resistive switching behavior, transitioning from a high-resistance state (HRS) to a low-resistance state (LRS). The SET process occurred at approximately 0.5 V, while the RESET process took place under a reverse bias of about −0.75 V. This low-voltage operation, along with a clear distinction between the HRS and LRS, highlights the devices' potential for low-power nonvolatile memory applications.

Electrical transport analysis indicates that the conduction mechanism adheres to a space-charge-limited current (SCLC) model, with ohmic conduction dominating the HRS at low voltages (0–0.4 V), followed by trap-controlled SCLC ($I \propto V^2$) and a trap-filled limit at higher fields, before reverting to ohmic behavior in the LRS. In addition to electrical switching, the devices demonstrated reversible optical modification of resistive states. Illumination with circularly polarized light reduced the conductance by nearly one order of magnitude, shifting the *I–V* characteristics to lower current levels due to photomechanical expansion of the polymer matrix, while subsequent exposure to linearly polarized light restored the original conductance through polymer contraction. This reversible optical control was particularly pronounced at $R_m = 0.05$ wt%, when conducting pathways were most susceptible to interruption. The observed behavior was attributed to *trans-cis-trans* photoisomerization within the polymer, resulting in thickness changes that disrupt or reconnect ZnO nanoparticle percolation pathways, rather than traditional ZnO photoconductivity effects.[118] This work examined how different concentrations of graphene oxide (GO), specifically 1.5, 2.5, and 5%, affected the optical and luminescence properties of zinc oxide nanorods (ZnO NRs)/GO nanocomposites. Several important insights were gained from the analyses, including photoluminescence (PL) measurements and ultraviolet-visible (UV-Vis) absorption spectroscopy. First, the energy band gap of the ZnO nanorods remained constant regardless of the GO concentration. In comparison to pure ZnO NRs, the UV-Vis spectra of the nanocomposites exhibited a redshift in absorption peaks, with the strongest absorption occurring at approximately 370 nm. The estimated band gap values for the ZnO NR nanocomposites

were approximately 3.10 eV. Second, the PL spectra revealed a redshift and a notable decrease in intensity within the visible light range, indicating a charge transfer process. Along with broad visible emission bands spanning 500–650 nm, the PL spectra also displayed significant near-band-edge UV emission in the 350–400 nm range. Finally, the estimated chromaticity coordinates of the nanocomposites in the CIE 1931 color space were (0.33, 0.34). These values closely resemble those of pure white, so the authors mentioned that these nanocomposites may be suitable for a variety of optoelectronic applications, including commercial LED technologies.[119]

In conclusion, ZnO-based nanostructures possess tunable optoelectronic properties that can be systematically modified through controlled doping, composite engineering, and variations in nanoparticle concentration. These characteristics make them suitable for applications in photodetection, energy conversion, and resistive memory devices. However, their performance is significantly affected by factors such as the defect density, dopant concentration, and percolation thresholds, which can negatively impact charge-transfer efficiency and operational stability.

3.3 UV protection

Owing to their significant ultraviolet (UV) absorption and scattering properties, zinc oxide (ZnO) nanoparticles are frequently employed in a variety of applications, including sunscreens, UV-blocking coatings, textiles, and polymers. These nanoparticles contribute to photostability, thereby safeguarding both materials and human skin from UV-induced damage. Moreover, their integration into textiles and packaging materials not only enhances UV resistance but also prolongs the longevity of these products.

Zinc oxide nanoparticles (ZnO NPs) were applied to 100% of raw cotton to prepare untreated and treated cotton textiles to protect human skin from UV radiation. After that, UV-vis spectroscopy was used to evaluate the treatment results, quantifying the ultraviolet protection factor (UPF) and the percentage of transmitted radiation (%T). Cotton textiles treated with UPF 61.50% were detected to transmit 2.65% ultraviolet radiation. Consequently, untreated cotton textiles have 1.63% of UPF and transmit 74.56% of ultraviolet radiation. As a result, compared with untreated cotton textiles, treated cotton textiles are highly protective.[41] The treated fabrics demonstrated a higher level of UV protection than zinc oxide, with an increase in the UPF index corresponding to higher silver concentrations. Additionally, the materials exhibited a high ultraviolet protection factor (UPF) of 69.67 ± 1.53, indicating a remarkable UV-blocking ability.[53]

The production of nanoscale zinc oxide (ZnO) particles was investigated, along with their effectiveness for UV protection of cotton and polyester/cotton textiles. Untreated woven cotton displayed UPFs of 1.05 (UV-A) and 1.07 (UV-B), whereas untreated knitted cotton had UPFs of 0.98 (UV-A) and 1.00 (UV-B). The untreated woven polyester/cotton (P/C) blend had UPFs of 2.30 (UV-A) and 5.50 (UV-B), and the untreated knitted P/C blend had UPFs of 1.80 (UV-A) and 4.40 (UV-B). These values were significantly enhanced by the application of ZnO nanoparticles, produced using two distinct synthesis techniques (Z1 and Z2). Z1 treatment yielded UPFs of 4.92 (UV-A) and 5.23 (UV-B) for 100% woven cotton fabrics, whereas Z2 treatment resulted in UPFs of 8.45 (UV-A) and 10.29 (UV-B). For 100% knitted cotton materials, Z1 treatment achieved UPFs of 4.00 (UV-A) and 4.70 (UV-B), while Z2 treatment provided UPFs of 8.80 (UV-A) and 9.50 (UV-B). In the case of woven polyester/cotton blends, Z1 treatment produced UPFs of 10.23 (UV-A) and 15.76 (UV-B), and Z2 treatment yielded UPFs of 11.80 (UV-A) and 16.20 (UV-B). For knitted polyester/cotton blends, Z1 treatment resulted in UPFs of 9.62 (UV-A) and 14.53 (UV-B), while Z2 treatment achieved UPFs of 11.10 (UV-A) and 15.87 (UV-B).

Overall, ZnO nanoparticles synthesized using technique Z2 consistently exhibited higher UPF values than those produced with technique Z1. The treatment materials demonstrated exceptional wash fastness, showing "no significant change in sunscreen activity" after 25 washes. Additionally, woven fabrics consistently outperformed knitted fabrics in terms of UV blocking capabilities across all treatments.[120] ZnO-coated cotton textiles have been widely reported as highly effective multifunctional materials for UV protection and self-cleaning applications, demonstrating nearly perfect ultraviolet attenuation and substantial photocatalytic activity. The reported UV protection factor (UPF) values for ZnO-functionalized fabrics consistently exceed the criterion for "excellent protection" (UPFs > 50), with some systems reaching UPF values over 800 and even 1000. Such strong UV-shielding performance is associated with UV-A and UV-B blocking efficiencies nearing 99.9%, far surpassing uncoated cotton fabrics, which typically exhibit lower UPF values and visible photodegradation under prolonged light exposure. In addition to UV-blocking, ZnO-coated textiles show robust self-cleaning properties under solar irradiation through the photocatalytic degradation of organic stains. Optimized ZnO coatings have achieved discoloration efficiencies of approximately 70–73% for UV-sensitive dyes like methylene blue within the first hour of sunlight exposure, which rise to 84–90% after 24 hours. These degradation rates are nearly double those observed in previous textile-based photocatalytic systems. ZnO-functionalized fabrics demonstrate significantly better stain removal than uncoated cotton, even for more common pollutants, such as coffee stains. After 24 hours of light exposure, reported discoloration efficiencies exceeded 80%, whereas untreated materials showed little to no clearance. The development of hierarchical or flower-like ZnO nanostructures, which provide increased surface area, improved light harvesting, and more effective charge separation, is often credited with these enhanced performances.[121]

Cotton fabric coated with ZnO nanoparticles offers significantly better UV protection compared to untreated cotton fabric, as evidenced by lower UV transmittance values. This improvement indicates that the treated fabric is more effective at blocking harmful UV radiation. The UV protection properties were assessed by measuring the transmittance curves of samples using a PerkinElmer UV-visible spectrophotometer, model LAMBDA 1050+, at wavelengths ranging from 200 to 700 nm. The quantitative findings revealed a strong correlation between UV protection and ZnO nanoparticle concentration. For the untreated fabric, the transmittances were as follows: UV-

A (320–400 nm) at 60%, UV-B (280–320 nm) at 50%, and UV-C (200–280 nm) at 51%. In contrast, the transmittance dramatically decreased for textiles treated with ZnO nanoparticles. Specifically, Cot-1 (0.5% nano ZnO) showed a transmittance of 32% in the UV-B range, indicating 68% UV blockage, and 40% transmittance in the UV-A region, reflecting 60% UV light blocking. Cot-2 (1.0% nano ZnO) exhibited 78% UV blocking in the UV-B range, with a transmission of 22% in both the UV-A and UV-B regions. The highest concentration, Cot-3 (2.0% nano ZnO), yielded the best results with only 5% transmission in the UV-A region and 6% in the UV-B region, corresponding to an impressive 98% UV blockage in the UV-B range.

Overall, the fabric treated with 2% ZnO nanoparticles demonstrated approximately 96% UV blocking. Using published literature and the AS/NZS 4399 standard, these transmittance values were converted into Ultraviolet Protection Factor (UPF) ratings. Untreated fabric was classified as "Poor," with a UPF of 7 ± 2. Cot-2 (1.0% nano ZnO) received a "Good" rating with a UPF of 20 ± 4, while Cot-1 (0.5% nano ZnO) had a "Moderate" UPF of 12 ± 3. The Cot-3 sample (2.0% nano ZnO) achieved an average UPF of 31 ± 3, indicating "Very Good" UV protection. This demonstrates that increasing the concentration of nano zinc oxide significantly enhances the UV protection of cotton fabric.[122]

Strong and consistent UV protection is demonstrated by textiles coated with biofunctionalized zinc oxide (ZnO) nanoflowers, indicating their appropriateness for functional clothing applications. With approximately 92% UV-A and 94% UV-B attenuation, the treated fabrics showed significant UV blocking efficiency, above 90% overall, demonstrating the efficacy of the nanoflower shape in protecting against harmful radiation. When the ultraviolet protection factor (UPF) is quantitatively evaluated using transmission and erythemal spectral data, the result is a UPF value of approximately 15, which is within the "good" protection category (UPF 15–24) and equates to blocking approximately 93.3–95.9% of incident UV light. According to durability tests, the UPF decreased by approximately 13% after five cycles of washing in distilled water, but the fabric still has a significant amount of UV-blocking power. From a material standpoint, the ZnO nanoflowers' direct bandgap of roughly 3.25 eV in the UV region allows for effective UV photon absorption and electron–hole production, and their large surface area further improves UV absorption.[123] The study found that addition of zinc oxide (ZnO) nanoparticles to cotton fabric significantly improved its self-cleaning and UV protection qualities. For self-cleaning, the plasma-treated sample (P1) exhibited a photocatalytic efficiency of approximately 77%, while the citric acid-treated sample (P2) demonstrated a 63% efficiency in decomposing methylene blue. This self-cleaning effect is attributed to the ZnO photocatalyst's ability to produce electron–hole pairs when exposed to UV light, facilitating redox reactions that break down dye molecules. The plasma treatment further enhanced this effect by creating functional groups on the fabric's surface and increasing the density of the loaded ZnO nanoparticles.

The unloaded cotton fabric had UVA and UVB blocking percentages of 70.92% and 76.54%, respectively, resulting in an Ultraviolet Protection Factor (UPF) of 70.02 units. After loading ZnO, samples P1 and P2 exhibited significantly higher UPF values of 95.27 and 91.22, respectively. Specifically, UVB blocking was 94.11% for P1 and 92.65% for P2, while UVA blocking was 95.27% for P1 and 91.22% for P2. The pre-coating plasma treatment marginally improved the UV-blocking capacity of the ZnO-loaded cotton fabric.[124]

ZnO nanoparticle-functionalized textiles exhibit significantly enhanced ultraviolet (UV) protection, demonstrating substantial attenuation of both UV-A and UV-B radiation, with ultraviolet protection factor (UPF) values ranging from good to exceptional. This efficacy is attributable to robust UV absorption, scattering mechanisms, and specifically engineered nanostructured morphologies. Although increased ZnO loading, advanced nanostructures, and surface treatments enhance UV-blocking effectiveness and wash durability, overall performance is notably influenced by factors such as nanoparticle concentration, synthesis methods, fabric architecture, and coating uniformity. Future challenges include enhancing long-term durability, standardizing UPF assessments, and balancing UV protection with comfort, breathability, and environmental safety of fabrics for widespread textile applications.

3.4 Biomedical

ZnO NPs exhibit antimicrobial, antifungal, anti-inflammatory, and anticancer properties through mechanisms such as the generation of reactive oxygen species (ROS), the release of Zn^{2+} ions, and disruption of cell membranes. They are utilized in drug delivery, wound dressings, bio-imaging, and as antimicrobial coatings for medical devices. Antibacterial activity against *E. coli* (PTCC 1270) was tested and it was found that Cu-doped ZnO showed a higher antibacterial activity than undoped ZnO. Antibacterial activity was assessed against *E. coli* (PTCC 1270) bacteria for doped and non-doped zinc oxide using the agar diffusion method. The antibacterial activity was evaluated under both dark and visible light conditions. The authors reported that non-doped zinc oxide exhibited limited antibacterial activity in the dark (inhibition zone = 19.13 mm) and visible light (inhibition zone = 15.58 mm). Moreover, doping zinc oxide with copper at concentrations of 10% and 25% improves activity against *E. coli* under both light conditions. Specifically, the 10% Cu-doped zinc oxide demonstrated inhibition zones of 25.67 mm and 17.95 mm under dark and light conditions, respectively. Similarly, the 25% Cu-doped zinc oxide exhibited comparable inhibition zone values to those of the 10% Cu-doped variant, with measurements of 26.67 mm and 17.62 mm for dark (UV) and light conditions, respectively. These results suggest that the reduction in particle size and the narrowing of the energy band gap in doped zinc oxide contribute to improved antibacterial activity. Furthermore, the authors concluded that exposure of Cu-doped zinc oxide to light appears to enhance antibacterial efficacy, potentially through the activation of reactive oxygen species (ROS) production as described previously.[125]

The antibacterial activity of Mg doped and undoped ZnO NPs was evaluated against *S. aureus* bacteria and *E. coli* using the agar well diffusion method. The results indicated that the Mg-

doped ZnO NPs demonstrated zones of inhibition of 8.3 and 9.1 mm against *E. coli* and *S. aureus*, respectively, compared to undoped ZnO NPs that revealed zones of inhibition of 7.7 and 6.1 mm against the same strains, indicating that Mg doping had a positive effect against *S. aureus* bacteria and *E. coli*.[37]

Furthermore, the antimicrobial activity of co-doped ZnO NPs showed improvement in the antimicrobial activity against different pathogenic strains including two Gram-positive (*B. pumilis* and *E. faecalis*), two Gram-negative (*E. coli* and *E. cloacae*), and two fungal strains (*S. cerevisiae* and *C. albicans*). The authors evaluated the zone of inhibition, minimal inhibitory concentration (MIC), and minimal bactericidal and fungicidal concentration (MBC/MFC), and the results showed that the majority of these NPs demonstrated bactericidal and fungicidal properties. The authors reported that modification of ZnO with rare earth metals (La and Sm) and an alkali earth metal (Sr) enhanced antimicrobial activity. Finally, the authors conducted molecular docking simulations comparing pure and doped ZnO and demonstrated that the antibacterial activity was linked to the inhibition of DNA gyrase, the inhibition of cell wall synthesis (Upps and Fos A), and the inhibition of biofilm formation (PqsR). This analysis aimed to identify the appropriate mode of action responsible for bacterial inhibition, and the results indicated that co-doped nanoparticles exhibited higher binding energies than pure ZnO.[42]

Additionally, the antibacterial activity of double-doped ZnO incorporating iron and aluminum was evaluated at three concentrations (5, 15, and 25 mg mL^{-1}) against *E. coli, B. subtilis*, and *S. aureus*. The results indicated that the zone of inhibition increased with higher concentrations of the doped particles and with an increased concentration of aluminum in the doped samples, suggesting that the bacterial inhibition is influenced by a concentration-dependent effect. The synthesized nanoparticles exhibited enhanced antibacterial activity, especially against *S. aureus*. Additionally, the antioxidant activity was determined using the DPPH assay concentrations (25, 50, 100, 200, 400, and 800 μg mL^{-1}), compared to ascorbic acid. The results indicated that all samples exhibited significant antioxidant activity with the sample containing a high concentration of aluminum demonstrating strong scavenging activity. The percentage values ranged from 11.72 to 88.41%, compared to ascorbic acid (15.56–90.49%).[50]

Furthermore, the synthesized ZnO nanoparticles exhibited significant antioxidant properties with inhibitory percentage values of 85.75 ± 0.33 and 90.23 ± 0.82% at concentrations of 40 and 50 μg mL^{-1}, respectively. In comparison, ascorbic acid displayed inhibitory percentages of 87.89 ± 1.34 and 91.23 ± 0.82% at the same concentrations. Additionally, the IC_{50} values were calculated and the results showed that ZnO NPs had an IC_{50} value of 6.33 ± 3 μg mL^{-1}, whereas ascorbic acid exhibited an IC_{50} value of 5.40 ± 3 μg mL^{-1}. These results indicate that ZnO NPs possess robust antioxidant activity, comparable to that of the standard drug ascorbic acid. Additionally, the anti-inflammatory activity of ZnO NPs was evaluated by a membrane stabilization assay, and the results revealed that ZnO exhibited an effect of 53.05 ± 1.06%, which was slightly lower than that of sodium diclofenac, which had an inhibitory percentage value of 57.14% ± 0.91% at 10 μg mL^{-1}. Moreover, the authors reported that at high concentrations of 40 and 50 μg mL^{-1}, the ZnO NPs showed an inhibitory percentage that was comparable to or even exceeded that of diclofenac sodium in terms of membrane stabilization. The antibacterial activity of ZnO NPs was evaluated against various wound pathogens, including *Pseudomonas* species, *E. coli*, and *S. aureus* at different concentrations (25, 50, and 100 μg mL^{-1}) and exhibited significant antibacterial activity as well as inhibited the formation of biofilms. The ZnO NPs were evaluated in time-kill assays against three wound pathogens: *S. aureus*, *P. aeruginosa*, and *E. coli*. The results showed a significant reduction in bacterial count. A study on the toxicity of zebrafish embryonic nanoparticles revealed minimal toxicity at concentrations ranging from 5 to 20 μg mL^{-1}; however, higher concentrations (40 to 80 μg mL^{-1}) negatively impacted hatching and survival rates. In addition to promoting accelerated tissue regeneration, *in vitro* wound healing assays demonstrated enhanced migration and proliferation of fibroblasts.[51]

The coated ZnO and Ag/ZnO nanocomposites demonstrated excellent antibacterial activity, particularly against *S. aureus*, which persisted even after 20 wash cycles. Firstly, the antibacterial activity of fabric-coated ZnO and Ag/ZnO nanocomposites was evaluated against *S. aureus* and *E. coli* using the agar well diffusion method. The results revealed that modifying ZnO with silver to form Ag/ZnO NPs produced strong antibacterial activity, with inhibition zone (IZ) values of 26.21 ± 1.53 mm against *S. aureus* and 13.02 ± 1.00 mm against *E. coli*. In contrast, the ZnO NPs exhibited no zone of inhibition under the same conditions. Furthermore, treating the fabric with Ag/ZnO NPs resulted in excellent zones of inhibition, measuring 55.48 ± 2.52 mm against *S. aureus* and 36.24 ± 2.08 mm against *E. coli*.[53]

Furthermore, it was reported that the synthesized flower-like zinc oxide nanostructures demonstrated good antibacterial activity with an MIC/MBC value of 25 mg L^{-1} against *E.* coli (strain ATCC 25922) and *S. aureus* (strain ATCC 25923).[55] Besides, the synthesized copper-doped and undoped ZnO NPs, used as new anticancer agents against G-292 (bone cancer) and MRC-5 (normal lung fibroblast) cells after 24 and 72 h of exposure, were evaluated for their cytotoxic and anticancer properties using both *in vitro* and *in vivo* assays. The Cu-doped ZnO nanoparticles exhibited greater cytotoxicity compared to the undoped ZnO and showed moderate anticancer activity against the tested cell lines.[56]

On the other hand, two types of ZnO NPs: one capped with poly(*N*-vinylpyrrolidone) (PVP) and the other without PVP, were used to assess the antifungal activity against *Phytophthora capsica*, which was isolated from infected pepper plants and measured as the percentage of growth inhibition (*E*%). The PVP-capped ZnONPs showed significant inhibition of fungal growth indicating that the activity increased with increasing the incubation time.[57] *In vitro* cytotoxicity of the nanocomposites (PEG/PVA/ZnO nanocomposites and PEG/PVA) was assessed using the MTT assay on MCF-7 cells. The results indicated that PEG/PVA/ZnO reduced cell viability to 91%, compared to 98% for PEG/PVA and 100% for the control group. This suggests that the presence of ZnO nanoparticles enhances the cytotoxic activity of

the nanocomposite. Furthermore, the application of PEG/PVA hydrogel encapsulated with ZnO nanoparticles shows significant promise for pH-sensitive controlled drug release.[69]

The leaf extract of *Senecio chrysanthemoides* was utilized as a reducing agent in the synthesis of biosynthesized ZnO NPs. Furthermore, researchers had compared the anti-inflammatory properties of biosynthesized ZnO NPs with those of diclofenac sodium using the heat-induced hemolysis method (human red blood cells). The experimental results demonstrated that the biosynthesized ZnO NPs exhibited significant anti-inflammatory activity at relatively high concentrations, achieving a 73.01% inhibition compared to that of the leaf extract (70.31%) and standard drug (86.71%), respectively.[97] Zinc oxide nanoparticles (ZnO NPs) were synthesized through a biosynthetic method with an extract derived from the leaves of *Veronica multifida*. The researchers tested the biosynthesized ZnO NPs on microorganisms to investigate their antimicrobial activities. The antimicrobial activity was evaluated against Gram-positive strains, including *S. aureus*, *B. subtilis*, and *B. licheniformis*, as well as Gram-negative strains such as *E. coli*, *P. aeruginosa*, and *S. typhimurium*, utilizing the agar well diffusion method. Notable antibacterial activity was observed at a concentration of 2.5 mg mL^{-1}. MIC and MBC were determined, revealing a pronounced bacteriostatic effect rather than a bactericidal effect on the tested strains. Additionally, the antibiofilm activity of ZnO NPs was assessed against *S. aureus* and *P. aeruginosa*, demonstrating inhibition of biofilm formation in a dose-dependent manner. Finally, the authors concluded that the biosynthesized ZnO NPs exhibited antimicrobial activity against both Gram-negative and Gram-positive bacteria and effectively inhibited the biofilm formation of *P. aeruginosa* and *S. aureus*.[98]

Furthermore, the biosynthesized ZnO NPs were prepared utilizing phytochemicals derived from an aqueous leaf extract of *Salvia officinalis* in conjunction with a zinc nitrate solution. The *in vitro* antifungal activity was evaluated against two standard *C. albicans* strains (coded as SC5314 and 4175) and one resistant isolate *C. albicans* (5112). The results revealed that ZnO NPs showed MIC values of 1.95 μg mL^{-1} against *C. albicans* (SC5314) and *C. albicans* (4175) compared to fluconazole, which exhibited MIC values of 0.25 and 0.125 μg mL^{-1} against the same strains. Moreover, the bio-fabricated ZnO NPs demonstrated an MIC value of 7.81 μg mL^{-1} and MFC value of 31.25 μg mL^{-1} compared to fluconazole (MIC = 64 μg mL^{-1}) against fluconazole-resistance strains. The authors further investigated the mechanism of action of ZnO NPs on antifungal activity by examining estrogen biosynthesis in various strains of *C. albicans*. Their findings revealed that bio-fabricated ZnO NPs significantly reduced estrogen biosynthesis in a dose-dependent manner compared to untreated control cells. Specifically, the study reported a decrease in ergosterol content of 59–69%, 63–74%, and 87–98% at 1/4 MIC, 1/2 MIC, and MIC of ZnO NPs, respectively. The morphological study using SEM on *C. albicans* (SC5314) was conducted with bio-fabricated ZnO NPs. The results showed a disruption of membrane integrity, indicating that the synthesized ZnO NPs exhibited multiple drug targets and were ultimately developed as a novel antifungal agent.[99]

On the other hand, the aqueous extract of *Punica granatum* peel for the biosynthesis of ZnO NPs was evaluated for their use as antimicrobial agents. The antimicrobial activity was tested using Gram-positive bacteria (*S. aureus* ATCC 6538 and *B. subtilis* ATCC 6633), Gram-negative bacteria (*P. aeruginosa* ATCC 9022 and *E. coli* ATCC 8739), and unicellular fungi (*C. albicans* ATCC 10231). The synthesized ZnO NPs exhibited their activity in a dose-dependent manner with MIC values ranging between 6.25 and 12.5 μg mL^{-1}. The bio-synthesized ZnO-NPs were highly effective against *P. aeruginosa*, as indicated by large inhibition zones and low MIC values. This was followed by notable activity against *S. aureus*, *E. coli*, and *C. albicans* under light conditions.[101] Additionally, through bio-reduction of zinc nitrate, zinc oxide nanoparticles were synthesized in the presence of the siderophore pyoverdine, which is produced by *Pseudomonas aeruginosa*. The synthesized ZnO NPs demonstrated significant antibacterial activity against both Gram-positive bacteria (*S. aureus* and *Bacillus* sp.) and Gram-negative bacteria, including *E. coli*. Additionally, they showed fungicidal effects against various phytopathogenic fungi, such as *Fusarium* sp., *Rhizoctoniasolani*, and *Penicillium* sp., and the results were obtained as zones of inhibition, which revealed that the activity increased with an increase in the concentration of ZnO (25–100 μg per well). With 100 μg of ZnONPs in an 8 mm agar well, the antibacterial activity exhibited a zone of inhibition of 28 mm against *Bacillus* sp., followed by 24 mm against *E. coli* and 21 mm against *S. aureus*. In terms of antifungal activity, the maximum zone of inhibition was observed against *R. solani* at 65 mm, followed by *Penicillium* sp. at 53 mm and *Fusarium* sp. at 48 mm.[107]

The *Bacillus cereus* strain was utilized to synthesize zinc oxide nanoparticles employing eighteen bacterial isolates. The antimicrobial activity of biosynthesized ZnO NPs was evaluated against three multidrug-resistant bacteria: *S. aureus* (BTCB203), *E. coli* (BTCB201), and *S. typhi* (BTCB202). The results indicated that the inhibitory effect of zinc oxide nanoparticles increased with concentration. For *E. coli*, the ZnO NPs demonstrated an 8-fold increase in activity at a concentration of 0.6 μg mL^{-1} compared to 0.1 μg mL^{-1}. In the case of *S. aureus*, the activity of the synthesized ZnO NPs resulted in an 11-fold increase in the inhibitory zone at a concentration of 0.3 μg mL^{-1}, whereas no zones of inhibition were observed at 0.1 and 0.2 μg mL^{-1}. Additionally, for *S. typhi*, the ZnO NPs at a concentration of 0.6 μg mL^{-1} produced an inhibitory zone of 24 mm, which was 1.71-fold greater than that observed at 0.2 μg mL^{-1}, whereas no inhibitory zone was detected at 0.1 μg mL^{-1}.[108]

The antibacterial activity of ZnO NPs derived from the cell-free supernatant (CFS) and cell biomass (CB), abbreviated as ZnO NPs-CFS and ZnO NPs-CB, was evaluated against Gram-negative bacteria (*E. coli* and *Salmonella* sp.) and Gram-positive bacteria (*S. aureus* and *S. epidermidis*) using the agar well diffusion method, with results expressed in millimeters (mm). This was followed by determining MIC and MBC expressed in μg mL^{-1}. As the concentration of ZnO NPs increased, the inhibitory effect also increased, indicating that

the biosynthesized ZnO NPs exhibited varying degrees of antibacterial activity.

Generally, ZnO NPs-CB exhibited higher activity than ZnO NPs-CFS, as indicated by the MIC values. ZnO NPs-CB showed the best MIC value against *S. aureus* (MIC = 312.5 μg mL^{-1}, MBC = 2500 μg mL^{-1}) and *E. coli* (MIC = 625 μg mL^{-1}, MBC = 8000 μg mL^{-1}), while ZnO NPs-CFS had MIC values of 2500 μg mL^{-1} against *S. aureus* and *S. epidermidis*, and 2500 μg mL^{-1} against *E. coli* and *Salmonella* sp. The ZnO NPs-CFS revealed MBC values of 2500 μg mL^{-1} against *S. aureus* and *S. epidermidis*, while showing MBC values of 4000 μg mL^{-1} against *E. coli* and 8000 μg mL^{-1} against *Salmonella* sp. The biocompatibility of ZnO NPs-CFS and ZnO NPs-CB was assessed using the MTT assay on Vero cells. The results indicated IC50 values of 55.0 μg mL^{-1} for ZnO NPs-CFS and 100.0 μg mL^{-1} for ZnO NPs-CB, which may be attributed to the unique nanoflower morphology of the nanoparticles.[109] The antibacterial activity of the ZnO nanoparticles showed a clear inhibition zone when tested against the bacterial phytopathogen *Xanthomonas oryzae* pv. oryzae at a concentration of 100 μg mL^{-1}. However, at lower concentrations, they did not produce distinct inhibition zones. In addition, the antifungal activity of ZnO nanoparticles was evaluated against *Alternaria* sp., and the results demonstrated a dose-dependent inhibition of fungal growth, with maximum inhibition of 92.22% observed at 250 μg mL^{-1}.[110]

Furthermore, the biological activity of the synthesized ZnO-NPs against pathogenic microbes, including both Gram-positive and Gram-negative bacteria, as well as fungal strains, was accessed and the results showed that the ZnO NPs exhibited significantly higher antibacterial efficacy compared to bulk zinc acetate ($Zn(CH_3COO)_2 \cdot 2H_2O$). The antimicrobial activity of the ZnO-NPs was evaluated using the agar well diffusion method, revealing their effectiveness against pathogenic microbes. At a concentration of 200 ppm, the measured zones of inhibition were as follows: *S. aureus* 12.3 ± 0.9 mm, *B. subtilis* 29.3 ± 0.3 mm, *E. coli* 19.2 ± 0.3 mm, *P. aeruginosa* 11.7 ± 0.2 mm, and *C. albicans* 22.3 ± 0.3 mm. The synthesized ZnO NPs demonstrated MIC values of 200 ppm against *P. aeruginosa* and *S. aureus* while exhibiting MIC values of 50 ppm for C. albicans, *E. coli*, and *B. subtilis*. The biosynthesized ZnO nanoparticles exhibited markedly higher mortality rates in *Culex pipiens*, achieving a mortality rate of 100 ± 0.0% at a concentration of 200 ppm after 24 hours. In comparison, zinc acetate at the same concentration and duration induced a mortality rate of only 44.3 ± 3.3%.[111]

Zinc oxide (ZnO)-based nanomaterials are characterized by a diverse array of biological activities, which encompass antibacterial, antifungal, anti-inflammatory, antioxidant, and anticancer properties. These activities are primarily attributed to mechanisms such as the generation of reactive oxygen species, the release of Zn^{2+} ions, and the disruption of cellular and biomolecular structures. Various techniques, including doping, co-doping, surface modification, and bio-fabrication, have been employed to enhance their biological efficacy. However, the performance of these nanomaterials is significantly influenced by several factors, including nanoparticle concentration, morphology, and exposure conditions, with toxicity becoming evident at elevated doses. Although these materials demonstrate substantial *in vitro* efficacy, their limited effectiveness *in vivo*, coupled with variability in biological assays and dose-dependent safety concerns, poses significant challenges that continue to impede their potential for biomedical applications.

3.5 Industrial

Zinc oxide nanoparticles (ZnO NPs) are extensively utilized in various industrial applications, including rubber, plastics, adhesives, coatings, and chemical catalysis. They function as ultraviolet (UV) stabilizers, antimicrobial agents, and functional fillers, thereby improving the performance and durability of industrial products. Furthermore, ZnO NPs are employed in sensor technology and packaging materials to increase food safety.

The ZnPCP (ZnO@plant polyphenols/cellulose/polyvinyl alcohol) bio-composite material has been developed as an innovative active food packaging solution, offering numerous advantages for extending food shelf life and ensuring safety. Its antibacterial properties, improved water resistance, light-shielding capabilities, antioxidant effects, and ability to preserve food freshness make it particularly suitable for food packaging applications. ZnPCP films exhibit exceptional UV and visible light shielding properties. The bio-composite significantly diminishes light transmission, whereas a pure polyvinyl alcohol (PVA) film permits approximately 80% UV light and 90% visible light to pass through. Plant polyphenols (PPLs) alone provide adequate light shielding; however, at a modest dosage of 0.2 weight percent ZnO@PPL/cellulose (ZnPCP-2), only 3% of UV light and 25% of visible light can penetrate the film. Increasing the dosage to 0.8% (ZnPCP-8) and 1% (ZnPCP-10) ZnO@PPL/cellulose enhances the films' capability to block nearly all UV and visible light. This improved light shielding is instrumental in preventing food deterioration resulting from light exposure.

ZnPCP films exhibit strong antibacterial activity against common food spoilage bacteria, particularly Gram-positive *S. aureus* and Gram-negative *E. coli*. In contrast, the PVA film shows minimal antibacterial activity. The ZnPCP-10 film, with the highest concentration, displays the most significant antibacterial effects, with inhibition zones of 4.4 mm against *E. coli* and 6.3 mm against *S. aureus*. This efficacy is attributed to the combined action of cellulose, ZnO (which generates reactive oxygen species), and PPL (which contains phenolic groups). The water content of ZnPCP films was approximately 9.4%, similar to that of PVA (9.86%), indicating that the addition of ZnO@PPL/cellulose has a negligible effect on the water content. However, compared with PVA, ZnPCP films exhibited reduced water solubility (ranging from 8.9% to 6.6% with increasing dosage), suggesting enhanced water resistance due to interactions between PPL, cellulose, and PVA.

Furthermore, ZnPCP films possess superior water-vapor barrier properties compared with those of PVA. The water vapor permeability (WVP) for PVA is 12.7 g m^{-2} h^{-1}, whereas for ZnPCP films it ranges from 10.8 to 7.5 g m^{-2} h^{-1}. A lower WVP minimizes water transfer between food and the environment, which is essential for food preservation. The antioxidant activity

of the films was evaluated by their ability to scavenge DPPH free radicals. The ZnPCP-10 film exhibited a radical scavenging activity of 40.2%, indicating good oxidation resistance and the potential to extend food shelf life. Compared to control or PVA-packaged apple slices, ZnPCP films significantly reduced weight loss and delayed browning. Apple slices in PVA bags showed noticeable caramelization after 48 hours, while those exposed to air browned within 24 hours. In contrast, apple slices wrapped in ZnPCP film only slightly browned after 72 hours, demonstrating superior food preservation capabilities.[126]

Gelatin films containing 10% nanofibers and 5% ZnO nanoparticles exhibited significant antibacterial activity while maintaining the organoleptic characteristics of cheese and chicken fillets. Bovine skin gelatin composite films containing 2% zinc oxide nanorods (under 100 nm) and clove essential oil enhanced shrimp shelf life. Carboxymethyl cellulose (CMC) coatings with varying ZnO nanoparticle concentrations (0, 5, 10, 20, and 40% w/v) effectively reduced fungal growth and black spots on tomato and persimmon fruits, using ZnO nanoparticles with a size range of 25–55 nm. CMC, okra mucilage, and ZnO nanoparticle-containing nanocomposite films also prolonged the shelf life of chicken breast meat. Chitosan–cellulose acetate phthalate films with 5% ZnO nanoparticles (30 nm) extended black grapefruit shelf life by up to nine days. Chitosan/CMC/ZnO films containing 2%, 4%, and 8% ZnO nanoparticles extended the shelf life of Egyptian soft white cheese for 30 days of storage at 7 °C. Polybutylene succinate (PBS) composite films with 2 to 10 weight percent ZnO nanoparticles (10 nm) produced inhibition zones of 1.31 cm and 1.25 cm, respectively, with 6% ZnO nanoparticles needed to inhibit *E. coli* and *S. aureus*.

Otolithes ruber fish, which demonstrated reduced Zn^{2+} migration below standard limits, experienced an extension of their shelf life through the application of PLA/ZnO nanoparticles infused with essential oils. The shelf life of green grapes was significantly prolonged by agar-ZnO nanocomposite films, characterized by an average ZnO nanoparticle size of 24.75 ± 0.78 nm; films incorporating 2% and 4% ZnO nanoparticles maintained a fresh appearance for durations of up to 14 and 21 days, respectively. Over a storage period of 72 days, semolina flour films containing rod-type ZnO (50–100 nm in diameter and 0.5–2 μm in length) and nano kaolin effectively inhibited microbial growth while preserving the sensory attributes of mozzarella cheese. LDPE/ZnO nanocomposites, containing 1%, 3%, and 5% ZnO nanoparticles in conjunction with 10% polyethylene-grafted maleic anhydride, extended the shelf life of strawberries in petroleum-based applications, maintaining microbial counts below 5 log CFU g^{-1} for 16 days. Additionally, the shelf-life of fresh lemon juice was enhanced by the addition of 70-nm ZnO nanoparticles to polypropylene (PP) sheets at concentrations of 0.5, 1, 3, and 5%.[127]

A recent study reported the presence of nanoparticles in all twenty cosmetic products examined. Specifically, fifteen samples of zinc oxide (ZnO) and nineteen samples of titanium dioxide (TiO2) were found to comply with the European Union criteria for nanomaterials, which stipulates that more than fifty percent of the particles must be smaller than 100 nanometers. The TiO_2 nanoparticles exhibited geometric mean diameters ranging from 71.4 to 112 nanometers, with weight concentrations between 1% and 30.7%. In contrast, the ZnO nanoparticle concentration ranged from 1% to 9.14%, and the geometric mean diameter ranged from 57.7 to 144.4 nm.[128] By altering synthesis parameters, such as the choice of starting materials, potassium hydroxide (KOH) concentration, and input speed, researchers have successfully synthesized various morphologies of ZnO particles, including needle-, planar-, and vertical-wall types. The D50 (average particle size) values for the produced non-nanosized particles ranged from 0.13 μm for low aspect ratio (LAR) needle-type ZnO to 0.36 μm for high aspect ratio (HAR) planar-type ZnO. Specifically, HAR needle-type ZnO measured 400 nanometers in length and 50 nanometers in thickness, while LAR needle-type ZnO measured 100 nanometers in length and 50 nanometers in thickness. The planar-type ZnO particles exhibited lengths ranging from 200 to 700 nanometers and thicknesses between 15 and 30 nanometers, with vertical wall-type ZnO particles measuring 150 nanometers in length and 20 nanometers in thickness. All measurements confirmed that these particles adhered to non-nanosized standards by exceeding 100 nanometers in all dimensions.

Furthermore, the synthesized powders exhibited higher crystallinity than commercially available nanosized zinc oxide (ZnO). The individual ZnO powders demonstrated significant light absorption and ultraviolet (UV) blocking efficiency. Within the 200–600 nm wavelength range, low aspect ratio (LAR) needle-type ZnO achieved the highest light absorption rate at 98.1%, while the high aspect ratio (HAR) planar-type ZnO exhibited the lowest absorption rate at 82.7%. The vertical wall-type particles absorbed 93.2% of the light. In contrast to bulk ZnO, which possesses an optical band gap (E_g) of approximately 3.37 eV, the synthesized powders exhibited a band gap range of 3.06 to 3.15 eV. A 1 : 1 combination of LAR needle-type ZnO and vertical wall-type ZnO demonstrated remarkable performance in cosmetic formulations. This blended powder achieved low light transmission rates of 1.7% in the UVB range and 3.8% in the UVA range, providing excellent light-blocking capabilities. The 1 : 1 blended powder resulted in a sun protection factor (SPF) of 40.3 ± 2.6 (SPF40) and a Protection Grade of UVA (PA) of 8.2 ± 1.2 (PA+++) in *in vivo* testing.[129]

Recent research has identified zinc oxide–cellulose nanofiber (ZnO–CNF) hybrid materials as highly promising candidates for cosmetic applications, particularly in sunscreen formulations, due to their improved safety profiles and superior optical performance. The ZnO–CNF hybrids achieved enhanced safer-by-design structures, resulting in high absorbance values of approximately 3.05 a.u. in the UV-B region and 2.80 a.u. in the UV-A region, demonstrating exceptional UV-blocking efficiency. This improved shielding efficacy is primarily due to the controlled size and uniform distribution of ZnO nanoparticles adsorbed onto the CNF surface, which enhances UV absorption while minimizing aggregation. Notably, the ZnO–CNF hybrid exhibited minimal photocatalytic activity, degrading rhodamine B by only 8.8% under irradiation, indicating limited production of reactive species. Such inhibited photocatalysis is critical for cosmetic safety, as UV filters with high photocatalytic

activity can exacerbate skin photodamage and compromise formulation integrity. The CNF matrix serves as both a physical and chemical barrier, restricting radical production by preventing charge transfer from photoexcited ZnO. Additionally, the high aspect ratio and network structure of CNFs likely impede the penetration of ZnO nanoparticles into the skin, addressing a significant safety concern associated with nanoscale UV filters.[130]

The nanoparticle-polymer composite of zinc oxide (ZnO) exhibited multifunctional properties, encompassing robust antibacterial efficacy, antioxidant capabilities, and improved water and light barrier performance, thereby rendering it an exemplary candidate for active food packaging applications. Its ability to block ultraviolet and visible light, reduce water vapor permeability, and mitigate food browning surpasses that of traditional packaging materials. Empirical evidence from analogous nanoparticle-polymer systems indicates that particle size, shape, and concentration play significant roles in determining antibacterial activity and extending shelf life. Nonetheless, challenges remain in achieving uniform distribution of nanoparticles and ensuring consistent performance across diverse food matrices.

3.6 Agriculture

In agriculture, zinc oxide nanoparticles (ZnO NPs) are used as nanofertilizers, seed priming agents, and foliar applications. These nanoparticles have been shown to enhance germination rates, promote vegetative growth, increase tolerance to abiotic stresses such as drought and salinity, and simultaneously improve nutrient uptake. Moreover, ZnO NPs offer protection against a range of plant pathogens and play a significant role in the remediation of agronomic soils.

The use of nanoscale ZnO particles as seed treatments resulted in significant, concentration-dependent enhancements in the performance of fodder maize. Coating seeds with 20 mg L^{-1} ZnO NPs resulted in the most substantial improvements in vegetative growth, as evidenced by the highest measurements of plant height, shoot biomass, fresh root weight, and total stover yield, surpassing both bulk $ZnSO_4$ and untreated control groups. Furthermore, seed coating demonstrated greater efficacy than seed priming in increasing leaf number and plant height. ZnO nanoparticles applied at a concentration of 40 mg L^{-1} maximized the availability of soil nitrogen (N), phosphorus (P), and potassium (K), whereas the 20 mg L^{-1} concentration resulted in the highest soil zinc (Zn) content. Both ZnO nanoparticles and bulk $ZnSO_4$ treatments effectively increased NPK and Zn concentrations in maize shoots and roots. Seed priming increased neutral detergent fiber and hemicellulose content, while seed coating raised acid detergent fiber and cellulose levels; notably, ZnO nanoparticles at 40 mg L^{-1} significantly increased both neutral detergent fiber and cellulose. Photosynthetic pigments, including total chlorophyll and carotenoids, reached their peak levels at 60 days post-sowing, particularly in response to the 20 mg L^{-1} ZnO NP treatment. The addition of 40 mg L^{-1} ZnO nanoparticles to the soil significantly enhanced nutrient availability and biological activity, leading to increased levels of available N, P, K, and Zn, as well as higher populations of beneficial microorganisms (including bacteria, fungi, pseudomonas, actinobacteria, and non-symbiotic nitrogen fixers), and improved activities of dehydrogenase, acid phosphatase, and alkaline phosphatase.[131]

The application of ZnO nanoparticles at various concentrations significantly enhanced wheat growth, productivity, and physiological functions. At a concentration of 25 mg L^{-1}, plant height increased by 23%, whereas increases of 13.8, 10.7, and 21.4% were observed at 50, 100, and 200 mg L^{-1}, respectively. The number of leaves increased by 32% at 25 mg L^{-1}, 12% at 50 mg L^{-1}, and 8% at 200 mg L^{-1}. Leaf area exhibited substantial increases of 153% at 25 mg L^{-1}, 83% at 50 mg L^{-1}, and between 104% and 129% at 100–200 mg L^{-1}. Root and shoot growth were significantly stimulated, with root length increasing by up to 93% at 200 mg L^{-1} and shoot length increasing by 30–38.9% across the 25–200 mg L^{-1} treatments. Biomass accumulation improved markedly with increasing ZnO nanoparticle concentration, with fresh weight increases ranging from 18% to 241% and dry weight increases ranging from 38% to 194.3%. Yield-related characteristics also showed improvements, including spike length (up to 27.2% at 25 mg L^{-1}), spikelets per spike (up to 25% at 200 mg L^{-1}), grains per spike (ranging from 108% to 235% across treatments), and grain weight (an increase of 15.4% to 42%). Chlorophyll content increased by up to 57%, carotenoid levels rose by 62% to 196%, and grain protein content increased by 26.8% at 100 mg L^{-1}. Proline content increased by up to 3.5%, while the activities of antioxidant enzymes such as peroxidase (12% at 50 mg L^{-1}), superoxide dismutase (up to 79.7% at 100 mg L^{-1}), and catalase (up to 39% at 50 mg L^{-1}) demonstrated significant stimulation, indicating an enhancement of stress-related metabolites and antioxidant defenses.[132]

Approximately one-third of arable soils worldwide are deficient in zinc, which adversely affects human nutrition. In soils located in arid regions, the availability of zinc typically ranges from 0.1 to 2.0 mg kg^{-1}. Excessive application of phosphate fertilizers can exacerbate zinc deficiency in plants, leading to imbalanced nutrient levels. Zinc plays a critical role in over 300 physiological processes and is an essential trace element for plant growth. Research indicates that the topical application of ZnO nanoparticles is more effective than traditional soil application for enhancing crop yield. Specifically, the application of 50 ppm ZnO nanoparticles in conjunction with the maximum recommended dose of phosphorus fertilizer (100% P) yielded a significant increase in crop productivity, with yields 1.4 times greater than those of the control treatment with 100% P alone and 1.9 times greater than the control treatment lacking both zinc and phosphorus. Under these conditions, soybean grain yields reached 2369.4 kg fed^{-1}, while wheat yields increased to 6171 kg fed^{-1}.

Furthermore, the application of ZnO nanoparticles improved crop quality by increasing the levels of protein, carbohydrates, crude lipids, nitrogen, phosphorus, potassium, and zinc in both soybean and wheat. The oil content in soybeans increased to 22.83% and 23.09% with foliar applications of 5 mg L^{-1} and 50 mg L^{-1} nano zinc, respectively, whereas protein content increased to 39.29% and 39.48%. In wheat, the carbohydrate

content reached 74.96% and 74.68%, and the protein content reached 13.42% and 13.29% with the foliar application of 50 mg L^{-1} nano Zn and 100% P. Post-harvest soil analysis revealed that the incorporation of nano Zn and phosphorus fertilizers increased the soil concentrations of zinc and phosphorus. In contrast, foliar spraying resulted in minimal changes in soil nutrient levels, accompanied by a slight reduction in nitrogen concentration.[133]

The application of ZnO nanoparticles showed dose-dependent effects on soil properties, nutrient accumulation, and potato performance. Low treatment rates ($\leq$200 mg kg^{-1}) significantly enhanced vegetative growth, increasing plant height by 23.11% and leaf dry weight by 19.90%. In contrast, higher concentrations ($\geq$500 mg kg^{-1}) decreased growth indices. Mean tuber weight increased with ZnO NP treatments, but overall biomass production and the number of tubers per plant declined. The highest dose (800 mg kg^{-1}) produced fewer tubers but resulted in the highest individual tuber mass, a 56.61% increase compared to the control. All treatments with ZnO NPs improved marketable production by shifting the tuber size distribution toward larger tubers, with the 200 mg kg^{-1} treatment yielding the most balanced results. Zinc concentrations in potato tissues increased in line with ZnO NP concentration, peaking at 800 mg kg^{-1}. Notably, zinc accumulation increased by 1915% in roots, 2140% in stems, 514% in leaves, 1970% in stolons, and 149% in tubers compared to the control group. Soil analyses indicated that the highest dosage of ZnO NPs increased soil pH and decreased total organic carbon by 13.33%, while all treatments led to a reduction in soil ammonium-N and nitrate-N, without significantly affecting total nitrogen levels. The 500 mg kg^{-1} treatment increased available soil phosphorus to 1.25 times the control value. Low ZnO NP application (50 mg kg^{-1}) slightly increased bacterial diversity, whereas higher concentrations suppressed it. Additionally, ZnO NP treatments reduced fungal diversity compared to the control.[134]

Salinity stress negatively impacts the growth of wheat and rice by increasing Na^+ accumulation in roots, shoots, and grains by up to threefold. This stress also resulted in decreased K^+ levels and a reduced K^+/Na^+ ratio, disrupting nutrient balance and adversely affecting crop production. Furthermore, zinc deficiency exacerbated reductions in crop yields, particularly in cereal-based diets, despite zinc's critical role in over 300 enzymatic and structural processes in plants. The application of ZnO nanoparticles (20–60 nm in size, with an average crystallite size of approximately 22.96 nm and spherical particles averaging 51 nm) significantly improved zinc biofortification and overall plant performance under both normal and saline conditions, outperforming traditional zinc sources. Under salinity stress, the grain zinc concentration in wheat increased from 18.5 to 45.7 mg kg^{-1} with ZnO-NP treatment, whereas it increased from 25.6 to 52.9 mg kg^{-1} under normal conditions. In rice, the shoot zinc concentration increased from 15 to 25 mg kg^{-1} under saline stress and from 22 to 34 mg kg^{-1} under nonsaline conditions. Additionally, the growth and yield characteristics significantly increased. Under normal conditions, the wheat plant height increased by 6.04%, the number of tillers per pot increased by 17.39%, the grain yield increased by 31.53%, and the total chlorophyll content increased by 7.25%. These benefits were even more pronounced under saline conditions. In rice, notable improvements included a 12.08% increase in shoot length, a 37.25% increase in the number of tillers per pot, a 64.66% increase in paddy yield, and a 5.08% increase in total chlorophyll content.[135]

Nanoscale ZnO particles consistently increase crop growth, yields, nutrient uptake, and stress tolerance across various plant species, demonstrating pronounced concentration-dependent effects. Foliar treatments and seed coatings generally exhibit greater effectiveness than soil applications and priming in improving vegetative growth, photosynthetic pigments, and biochemical markers, including antioxidant content and protein concentration. The observed increase in nutrient uptake correlated with increased soil microbial activity and enzyme function, leading to increased soil fertility and plant health. However, it is imperative to optimize dosage, as excessively high concentrations of ZnO nanoparticles may diminish growth indices, microbial diversity, and overall biomass. Collectively, these findings suggest that nanoscale ZnO has the potential to enhance crop productivity, nutritional quality, and resilience under both optimal and stress conditions.

4 Conclusion

In recent years, there has been growing scholarly interest in the green synthesis of zinc oxide nanoparticles (ZnO NPs) using plant extracts and microorganisms, owing to their environmental sustainability, reduced toxicity, and cost-effectiveness. Bio-assisted synthesis offers enhanced sustainability and biocompatibility compared to traditional chemical methods, which often rely on hazardous reagents, while facilitating precise control over nanoparticle size, shape, and crystallinity. Research has demonstrated that reaction parameters, including the type of biological agent, pH, temperature, and concentration, significantly impact the size, shape, and uniformity of nanoparticles. Nevertheless, several challenges persist, including low yield, poor reproducibility, difficulties in scaling up production, and limited understanding of the mechanisms governing biomolecule-mediated reduction, capping, and stabilization. Future investigations should prioritize hybrid methodologies that enhance control over nanoparticle properties through mechanistic studies, rigorous improvements in biological procedures, and the ecological advantages of green synthesis in conjunction with the precision of chemical techniques. Moreover, the development of scalable, efficient, and environmentally benign ZnO nanoparticles for applications in energy, agriculture, medicine, and environmental remediation will necessitate interdisciplinary collaboration among chemists, materials scientists, biologists, and engineers. By bridging the gap between laboratory-scale research and industrial applications, these initiatives can ultimately augment the sustainability and efficacy of ZnO nanoparticles.

Conflicts of interest

The authors declare no conflicts of interest.

Abbreviations

ZnO NPs	Zinc oxide nanoparticles
XRD	X-ray diffraction
FESEM	Field emission scanning electron microscopy
SEM	Scanning electron microscopy
EDS	Energy dispersive spectroscopy
EDX	Energy-dispersive X-ray spectroscopy
XPS	X-ray photoelectron spectroscopy
UV-Vis	Ultraviolet-visible spectroscopy
FT-IR	Fourier-transform infrared spectroscopy
TEM	Transmission electron microscopy
BET	(Brunauer–Emmett–Teller) surface area analysis
DLS	Dynamic light scattering
PL	Photoluminescence spectroscopy
TGA/DTG	Thermogravimetric/differential scanning calorimetry analysis
TGA	Thermogravimetric analysis
ZP	Zeta potential
VSM	Vibrating-sample magnetometry
UV protection	Ultraviolet protection
SPR	Surface plasmon resonance
UPF	Ultraviolet protection factor
RR43	Reactive red 43 dye
MO	Methyl orange dye
MB	Methylene blue dye
PEG	Polyethylene glycol
PVP	Poly(*N*-vinylpyrrolidone)
Ppy	Polypyrrole
CZ	Cu_2O/ZnO
AZO	Aluminum-doped ZnO
CZH	ZnO/hydroxyapatite nanocomposite
DBS	Dodecyl benzene sulfonic acid sodium salt
DMF	Dimethylformamide
NaCl	Sodium chloride
$ZnCO_3$	Zinc carbonate
PS	*Pistia Stratiotes*
E. hirta	*Euphorbia hirta* extract
O. americanum	*Ocimum americanum* extract
W/O/W	Water/oil/water
QC	Quercetin
W/O	Water-in-oil
CTAB	Hexadecyltrimethylammonium bromide
TPR	Temperature-programmed reduction
HA	Hydroxyapatite
SBS	Sodium benzene sulfonate
E. coli	*Escherichia coli*
S. aureus	*Staphylococcus aureus*
CFS	Cell-free supernatant
CB	Cell-biomass
MIC	Minimum inhibitory concentration
MBC	Minimal bactericidal concentration
MFC	Minimal fungicidal concentration

Data availability

This review is based entirely on previously published data, which are cited and available in the referenced literature.

Acknowledgements

The authors extend their appreciation to the Deanship of Research and Graduate Studies at King Khalid University for funding this work through the Large Research Project under grant number RGP2/41/46.

References

1 Y. Sun, W. Zhang, Q. Li, H. Liu and X. Wang, *Adv. Sens. Energy Mater.*, 2023, **2**, 100069.
2 S. Jadoun, J. Yáñez, R. Aepuru, M. Sathish, N. K. Jangid and S. Chinnam, *Environ. Sci. Pollut. Res.*, 2024, **31**, 19123–19147.
3 R. R. Kumar, D. Punetha and S. K. Pandey, *Res Dev Material Sci.*, 2018, **3**(3), RDMS.000565.2018.
4 Y. S. Cheng, K. W. Lam, K. M. Ng, R. K. M. Ko and C. Wibowo, in *2008 AIChE Annual Meeting*, AIChE 100, Philadelphia, PA, United States, 2008.
5 G. I. Ali and S. A. Habeeb, *Res. Chem.*, 2025, 102351.
6 V. N. Hegde, Biomedical applications of ZnO nanoparticles: a paradigm shift in healthcare, *Letters in Applied NanoBioScience*, 2024, **13**(3), 132.
7 R. Verma, S. Pathak, A. K. Srivastava, S. Prawer and S. Tomljenovic-Hanic, *J. Alloys Compd.*, 2021, **876**, 160175.
8 A. Nawaz, A. Farhan, F. Maqbool, H. Ahmad, W. Qayyum, E. Ghazy, A. Rahdar, A. M. Díez-Pascual and S. Fathi-karkan, *J. Mol. Struct.*, 2024, **1312**, 138545.
9 S. Ahmed, M. Ahmad, B. L. Swami and S. Ikram, *J. Adv. Res.*, 2016, **7**, 17–28.
10 Y. Y. Chan, Y. L. Pang, S. Lim and W. C. Chong, *J. Environ. Chem. Eng.*, 2021, **9**, 105417.
11 M. T. El-Saadony, G. Fang, S. Yan, S. S. Alkafaas, M. A. El Nasharty, S. A. Khedr, A. M. Hussien, S. Ghosh, M. Dladla and S. S. Elkafas, *Int. J. Nanomedicine*, 2024, 12889–12937.
12 P. Maijan, T. Waen-ngoen, S. Suwanboon, S. Chantarak and S. P. Voravuthikunchai, *Inorg. Chem. Commun.*, 2024, **162**, 112086.
13 D. Kulkarni, R. Sherkar, C. Shirsathe, R. Sonwane, N. Varpe, S. Shelke, M. P. More, S. R. Pardeshi, G. Dhaneshwar and V. Junnuthula, *Front. Bioeng. Biotechnol.*, 2023, **11**, 1159193.
14 N. S. Alsaiari, F. M. Alzahrani, A. Amari, H. Osman, H. N. Harharah, N. Elboughdiri and M. A. Tahoon, *Molecules*, 2023, **28**, 463.
15 S. D. Shirsat, R. S. Mane and V. Achal, in *Solution Methods for Metal Oxide Nanostructures*, Elsevier, 2023, pp. 319–368.
16 R. Raliya and J. C. Tarafdar, *Agric. Res.*, 2013, **2**, 48–57.
17 M. Gambino, M. A. A. Ahmed, F. Villa and F. Cappitelli, *Int. Biodeterior. Biodegrad.*, 2017, **122**, 92–99.
18 M. Y. Al-darwesh, S. S. Ibrahim and M. A. Mohammed, *Results Chem.*, 2024, **7**, 101368.
19 S. Iravani, *Green Chem.*, 2011, **13**, 2638–2650.

20 S. Jafarzadeh, N. Oladzadabbasabadi, M. A. Dheyab, M. A. Lalabadi, S. Sheibani, M. Ghasemlou, Y. Esmaeili, C. J. Barrow, M. Naebe and W. Timms, *Ind. Crops Prod.*, 2025, **223**, 120108.
21 N. B. Mahmood, F. R. Saeed, K. R. Gbashi and U.-S. Mahmood, *Mater. Lett.:X*, 2022, **13**, 100126.
22 K. Kusdianto, D. F. Nugraha, A. Sekarnusa, S. Madhania, S. Machmudah and S. Winardi, in *IOP Conference Series: Materials Science and Engineering*, IOP Publishing, 2021, vol. 1053, p. 12024.
23 A. Kołodziejczak-Radzimska and T. Jesionowski, *Materials*, 2014, **7**, 2833–2881.
24 C. M. Vlăduț, O.-C. Mocioiu and E. M. Soare, *Gels*, 2023, **9**, 424.
25 R. I. Walton, *Chem. Eur. J.*, 2020, **26**, 9041–9069.
26 M. Ramesh, M. Anbuvannan and G. Viruthagiri, *Spectrochim. Acta, Part A*, 2015, **136**, 864–870.
27 S. Raha and M. Ahmaruzzaman, *Nanoscale Adv.*, 2022, **4**, 1868–1925.
28 S. V Gudkov, D. E. Burmistrov, D. A. Serov, M. B. Rebezov, A. A. Semenova and A. B. Lisitsyn, *Front. Phys.*, 2021, **9**, 641481.
29 J. Xu, Y. Huang, S. Zhu, N. Abbes, X. Jing and L. Zhang, *J. Eng. Fiber. Fabr.*, 2021, **16**, 15589250211046242.
30 M. T. Noman, N. Amor and M. Petru, *Crit. Rev. Solid State Mater. Sci.*, 2022, **47**, 99–141.
31 V. N. Kalpana and V. Devi Rajeswari, *Bioinorg. Chem. Appl.*, 2018, **2018**, 3569758.
32 R. F. Herin, A. S. S. Judit, S. Sebastiammal, S. Shabna, S. S. J. Dhas and C. S. Biju, *Regen. Eng. Transl. Med.*, 2025, **11**, 165–189.
33 E. K. Droepenu, B. S. Wee, S. F. Chin, K. Y. Kok and M. F. Maligan, *Biointerface Res. Appl. Chem.*, 2022, **12**(3), 4261–4292.
34 K. Vignesh, A. S. Nair, C. Udhayakeerthana and T. Kalaivani, in *IOP Conference Series: Materials Science and Engineering*, IOP Publishing, 2022, vol. 1219, p. 12019.
35 S. Behfar, M. Ghorbanpour and M. J. A. Alatabe, *Indian Chem. Eng.*, 2025, 1–10.
36 M. Benamara, K. I. Nassar, M. Essid, S. Frick, R. Rugmini, K. C. Sekhar and J. P. B. Silva, *J. Sol-Gel Sci. Technol.*, 2024, **111**, 553–565.
37 R. Shahriiari and M. Ghorbanpour, *J. Ultrafine Grained Nanostruct. Mater.*, 2024, **57**, 61–67.
38 F. Khamis, N. M. Degig, M. M. Allaham and M. S. Mousa, *Phys. Scr.*, 2024, **99**, 35008.
39 D. Chen, X. Jiao and G. Cheng, *Solid State Commun.*, 1999, **113**, 363–366.
40 D. Polsongkram, P. Chamninok, S. Pukird, L. Chow, O. Lupan, G. Chai, H. Khallaf, S. Park and A. Schulte, *Phys. B*, 2008, **403**, 3713–3717.
41 B. Bulcha, J. Leta Tesfaye, D. Anatol, R. Shanmugam, L. P. Dwarampudi, N. Nagaprasad, V. L. N. Bhargavi and R. Krishnaraj, *J. Nanomater.*, 2021, **2021**, 1–10.
42 M. Basseem, A. A. Emam, F. H. Kamal, A. M. Gamal and S. A. Abo Faraha, *Appl. Organomet. Chem.*, 2023, e7238.
43 J. C. Anaya-Zavaleta, A. S. Ledezma-Pérez, C. Gallardo-Vega, J. Rodríguez-Hernández, C. N. Alvarado-Canché, P. E. García-Casillas, A. de León and A. L. Herrera-May, *Technologies*, 2025, **13**, 18.
44 M. Anujency, M. M. Ibrahim, S. Vinoth, V. Ganesh and R. Ade, *J. Photochem. Photobiol., A*, 2024, **449**, 115379.
45 M. Basseem, A. A. Emam, F. H. Kamal, A. M. Gamal and S. A. Abo Faraha, *J. Mater. Sci.*, 2023, **1–27**.
46 Z. Li, K. Peng, N. Ji, W. Zhang, W. Tian and Z. Gao, *Nanoscale Adv.*, 2025, **7**, 419–432.
47 J. Wojnarowicz, T. Chudoba and W. Lojkowski, *Nanomaterials*, 2020, 1086.
48 I. E. Doicin, M. D. Preda, I. A. Neacsu, V. L. Ene, A. C. Birca, B. S. Vasile and E. Andronescu, *Appl. Sci.*, 2024, **14**, 7854.
49 S. Nayak, A. Chaudhari, B. Vaidhun and J. Excip, *Food Chem.*, 2020, **11**, 79–92.
50 N. Verma, D. Pathak, K. Kumar, K. Jeet, S. Nimesh, L. Loveleen, S. Kumar and N. Thakur, *Mater. Chem. Phys.*, 2025, **333**, 130422.
51 J. Nandhini, E. Karthikeyan, M. Sheela, M. Bellarmin, B. G. Kannan, A. Pavithra, D. S. Sri, S. S. Prakash and S. R. Kumar, *Intell. Pharm.*, 2025, **3**, 90–109.
52 K. Rustembekkyzy, M. Sabyr, Y. N. Kanafin, L. Khamkhash and T. S. Atabaev, *RSC Adv.*, 2024, **14**, 16293–16299.
53 P. Porrawatkul, R. Pimsen, A. Kuyyogsuy, N. Teppaya, A. Noypha, S. Chanthai and P. Nuengmatcha, *RSC Adv.*, 2022, **12**, 15008–15019.
54 R. E. Adam, G. Pozina, M. Willander and O. Nur, *Photonics Nanostructures: Fundam. Appl.*, 2018, **32**, 11–18.
55 K. M. Kumar, B. K. Mandal, E. A. Naidu, M. Sinha, K. S. Kumar and P. S. Reddy, *Spectrochim. Acta, Part A*, 2013, **104**, 171–174.
56 H. Ghaznavi, M. R. Hajinezhad, Z. Hesari, M. Shirvaliloo, S. Sargazi, S. Shahraki, E. A. Saberi, R. Sheervalilou and S. Jafarinejad, *BMC Cancer*, 2025, **25**, 37.
57 H. T. Truong and L. Q. Le, *Mater. Technol.*, 2025, **40**, 2439832.
58 M. I. Din, R. Khalid, Z. Hussain, S. Gul and A. Mujahid, *Desalin. Water Treat.*, 2024, **317**, 100002.
59 A. Rezaei, E. Katoueizadeh and S. M. Zebarjad, *Mater. Today Chem.*, 2022, **26**, 101239.
60 M. Zare, K. Namratha, K. Byrappa, D. M. Surendra, S. Yallappa and B. Hungund, *J. Mater. Sci. Technol.*, 2018, **34**, 1035–1043.
61 J. Li, Q. Wu and J. Wu, in *Handbook of Nanoparticles*, ed. M. Aliofkhazraei, Springer International Publishing, Cham, 2015, pp. 1–28.
62 Y. Huo, S. Xiu, L.-Y. Meng and B. Quan, *Chem. Eng. J.*, 2023, **451**, 138572.
63 M. Ravbar, K. Maver, T. Knaflič, I. Arčon, N. N. Tušar, U. L. Štangar and A. Šuligoj, *Appl. Surf. Sci.*, 2025, **681**, 161463.
64 A. Prayoga, F. A. Ihsan, M. H. Al-Farizi, J. F. Sumbowo, A. N. Firdaus, A. P. Wijaya, F. D. Naufal, S. A. Abrori, A. Nuruddin and G. Shukri, in *AIP Conference Proceedings*, AIP Publishing, 2024, vol. 3003.
65 M. Segovia, C. Sotomayor, G. Gonzalez and E. Benavente, *Mol. Cryst. Liq. Cryst.*, 2012, **555**, 40–50.

66 A. M. Mohammed, S. S. Mohtar, F. Aziz, M. Aziz, A. Ul-Hamid, W. N. W. Salleh, N. Yusof, J. Jaafar and A. F. Ismail, *Mater. Sci. Semicond. Process.*, 2021, **122**, 105481.
67 A. K. Ganguli, T. Ahmad, S. Vaidya and J. Ahmed, *Pure Appl. Chem.*, 2008, **80**, 2451–2477.
68 Ö. A. Yıldırım and C. Durucan, *J. Alloys Compd.*, 2010, **506**, 944–949.
69 A. Gholami, M. Pourmadadi, H. Abdouss, Z. Amiri, M. Abdouss, A. Rahdar, R. Behzadmehr and S. Pandey, *J. Mol. Liq.*, 2024, **410**, 125563.
70 J. Pawlonka, G. Słowik, W. Gac and T. Borowiecki, *Ann. Univ. Mariae Curie-Sklodowska, Sect. AA:Chem.*, **2013**, 68, DOI: 10.2478/umcschem-2013-0009.
71 S. López-Cuenca, L. A. Pérez Carrillo, M. Rabelero Velasco, R. Díaz de León, H. Saade, R. G. López, E. Mendizábal and J. E. Puig, *J. Nanomater.*, 2011, **2011**, 431382.
72 S. K. Lim, S. H. Hwang and S. Kim, *Cryst. Res. Technol.*, 2010, **45**, 771–775.
73 C. Xu, S. De, A. M. Balu, M. Ojeda and R. Luque, *Chem. Commun.*, 2015, **51**, 6698–6713.
74 X. Liu, Y. Li, L. Zeng, X. Li, N. Chen, S. Bai, H. He, Q. Wang and C. Zhang, *Adv. Mater.*, 2022, **34**, 2108327.
75 A. Stanković, L. J. Veselinović, S. D. Škapin, S. Marković and D. Uskoković, *J. Mater. Sci.*, 2011, **46**, 3716–3724.
76 C. R. Dumitrescu, F.-D. Gheorghe, M. Matei, L.-M. □tefan and E. Holban, *Environ. Earth Sci. Proc.*, 2025, **33**, 3.
77 M. K. Nazir, M. B. Taj, A. A. Al-Ghamdi, A. Almasoudi, F. M. H. AlSulami, H. M. Banbela, O. M. Ali, M. M. Ahmed, M. I. Khan and A. Shanableh, *Catalysts*, 2025, **15**, 284.
78 G. Otis, M. Ejgenberg and Y. Mastai, *Nanomaterials*, 2021, **11**, 238.
79 H. Benhebal, M. Chaib, T. Salmon, J. Geens, A. Leonard, S. D. Lambert, M. Crine and B. Heinrichs, *Alexandria Eng. J.*, 2013, **52**, 517–523.
80 S. Suwanboon, *Sci. Asia*, 2008, **34**, 31–34.
81 S. S. Khudiar, F. A.-H. Mutlak and U. M. Nayef, *Optik*, 2021, **247**, 167903.
82 A. Ejsmont and J. Goscianska, *Materials*, 2023, **16**, 1641.
83 M. Hasanpoor, M. Aliofkhazraei and H. Delavari, *Procedia Mater. Sci.*, 2015, **11**, 320–325.
84 G. Mano, S. Harinee, S. Sridhar, M. Ashok and A. Viswanathan, *Sci. Rep.*, 2020, **10**, 2224.
85 K. Arundhathi and D. U. Maheswari, *Int. J. Adv. Res. Eng. Technol.*, 2019, **10**, 205–208.
86 B. Bekele, A. Degefa, F. Tesgera, L. T. Jule, R. Shanmugam, L. Priyanka Dwarampudi, N. Nagaprasad and K. Ramasamy, *J. Nanomater.*, 2021, **2021**, 1–10.
87 Ö. A. Yıldırım and C. Durucan, *J. Mater. Res.*, 2012, **27**, 1452–1461.
88 Q. Meng, J. Cui, Y. Tang, Z. Han, K. Zhao, G. Zhang and Q. Diao, *Ceram. Int.*, 2019, **45**, 4103–4107.
89 L. Muñoz-Fernandez, A. Sierra-Fernández, O. Milošević and M. E. Rabanal, *Adv. Powder Technol.*, 2016, **27**, 983–993.
90 N. M. Shamhari, B. S. Wee, S. F. Chin and K. Y. Kok, *Acta Chim. Slov.*
91 Y. Mao, Y. Li, Y. Zou, X. Shen, L. Zhu and G. Liao, *Ceram. Int.*, 2019, **45**, 1724–1729.
92 M. Islam, M.-G. Jeong, F. Ghani and H.-G. Jung, *J. Electrochem. Sci. Technol.*, 2015, **6**, 121–130.
93 H. A. Salam, R. Sivaraj and R. Venckatesh, *Mater. Lett.*, 2014, **131**, 16–18.
94 S.-Y. Cheah, M. Aminuzzaman, Y.-K. Phang, S. C.-Y. Lim, M.-X. Koh, S. Djearamane, H. Subramaniam, B.-H. Lim, F. Li and L.-S. Wong, *Green Process. Synth.*, 2025, **14**, 20240246.
95 S. Rajeshkumar, C. Malarkodi, M. Vanaja and G. Annadurai, *J. Mol. Struct.*, 2016, **1116**, 165–173.
96 P. E. Ochieng, E. Iwuoha, I. Michira, M. Masikini, J. Ondiek, P. Githira and G. N. Kamau, *Int. J. Biochem. Phys*, 2015, **23**, e61.
97 S. Zahoor, S. Sheraz, D. F. Shams, G. Rehman, S. Nayab, M. I. A. Shah, M. Ateeq, S. K. Shah, T. Ahmad and S. Shams, *Biomed. Res. Int.*, 2023, **2023**, 3280708.
98 S. Ş. Doğan and A. Kocabaş, *Hum. Exp. Toxicol.*, 2020, **39**, 319–327.
99 M. A. Abomuti, E. Y. Danish, A. Firoz, N. Hasan and M. A. Malik, *Biology*, 2021, **10**, 1075.
100 F. N. Alharbi, Z. M. Abaker and S. Z. A. Makawi, *Inorganics*, 2023, **11**, 328.
101 A. Fouda, E. Saied, A. M. Eid, F. Kouadri, A. M. Alemam, M. F. Hamza, M. Alharbi, A. Elkelish and S. E.-D. Hassan, *J. Funct. Biomater.*, 2023, **14**, 205.
102 B. S. Adeleke, O. M. Olowe, M. S. Ayilara, O. A. Fasusi, O. P. Omotayo, A. E. Fadiji, D. C. Onwudiwe and O. O. Babalola, *Heliyon*, 2024, **10**, e39636.
103 S. Rani, P. Kumar, P. Dahiya, A. S. Dang and P. Suneja, *Front. Microbiol.*, 2022, **13**, 824427.
104 S. Ying, Z. Guan, P. C. Ofoegbu, P. Clubb, C. Rico, F. He and J. Hong, *Environ. Technol. Innov.*, 2022, **26**, 102336.
105 M. S. Samuel, M. Ravikumar, E. Selvarajan, H. Patel, P. S. Chander, J. Soundarya, S. Vuppala, R. Balaji and N. Chandrasekar, *Catalysts*, 2022, **12**(5), 459.
106 H. Bahrulolum, S. Nooraei, N. Javanshir, H. Tarrahimofrad, V. S. Mirbagheri, A. J. Easton and G. Ahmadian, *J. Nanobiotechnol.*, 2021, **19**, 86.
107 M. Barsainya and D. P. Singh, *J. Pure Appl. Microbiol.*, 2018, **12**(4), 2123–2134.
108 M. Iqtedar, H. Riaz, A. Kaleem, R. Abdullah, A. Aihetasham, S. Naz and S. Sharif, *Rev. Mex. Ing. Química*, 2020, **19**, 253–266.
109 H. Mohd Yusof, N. Abdul Rahman, R. Mohamad, U. H. Zaidan and A. A. Samsudin, *Sci. Rep.*, 2020, **10**, 19996.
110 D. Jain, Shivani, A. A. Bhojiya, H. Singh, H. K. Daima, M. Singh, S. R. Mohanty, B. J. Stephen and A. Singh, *Front. Chem.*, 2020, **8**, 778.
111 A. M. Abdo, A. Fouda, A. M. Eid, N. M. Fahmy, A. M. Elsayed, A. M. A. Khalil, O. M. Alzahrani, A. F. Ahmed and A. M. Soliman, *Materials*, 2021, **14**, 6983.
112 K. Manikandan, N. D. Kumar, R. Velmurugan, M. Gokulnath, S. Parvathy, M. Ayyar, M. Swaminathan, P. Prabhu, A. M. S. Alhuthali and M. H. Abdellattif, *Sci. Rep.*, 2025, **15**, 31819.

113 M. E. Elsisi, M. M. Mostafa, H. Abdella, A. E. Khalil and A. S. Soror, *Sci. Rep.*, 2025, **15**, 31669.
114 M. Farag, S. M. El-Dafrawy and S. M. Hassan, *J. Inorg. Organomet. Polym. Mater.*, 2024, **34**, 930–943.
115 S. W. Balogun, H. O. Oyeshola, A. S. Ajani, O. O. James, M. K. Awodele, H. K. Adewumi, G. A. Àlàgbé, O. Olabisi, O. S. Akanbi and F. A. Ojeniyi, *Heliyon*, 2024, **10**(9), e29452.
116 V. F. Nunes, P. H. P. Lima, J. P. S. Mota, F. N. A. Freire and A. S. Bezerra Sombra, *Discov. Electrochem.*, 2025, **2**, 15.
117 N. Munna, R. Abdur, R. Islam, M. S. Bashar, S. F. U. Farhad, M. Kamruzzaman, S. Aziz, M. A. A. Shaikh, M. Hossain and M. S. Jamal, *Nanoscale Adv.*, 2023, **5**, 4996–5004.
118 A. H. Jaafar, C. Lowe, A. Gee and N. T. Kemp, *ACS Appl. Polym. Mater.*, 2023, **5**, 2367–2373.
119 I. Boukhoubza, M. Khenfouch, M. Achehboune, L. Leontie, A. C. Galca, M. Enculescu, A. Carlescu, M. Guerboub, B. M. Mothudi and A. Jorio, *Nanomaterials*, 2020, **10**, 1532.
120 S. Kathirvelu, L. D'souza and B. Dhurai, *Indian J. Fibre Text. Res.*, 2009, **34**, 267–273.
121 A. Lawrynowicz, E. Palo, R. Nizamov and K. Miettunen, *J. Photochem. Photobiol., A*, 2024, **450**, 115420.
122 I. S. Tania, M. Ali and M. Akter, *J. Eng. Fiber. Fabr.*, 2022, **17**, 15589250221136378.
123 M. Joseph, V. P. N. Nampoori and M. Kailasnath, *Mater. Today Proc.*, 2022, **68**, 363–366.
124 M. Irfan, H. Hussain, B. Saleem, M. Saleem, S. Shukrullah, S. Legutko, J. Petrů, M. Y. Naz, M. Pagáč and S. Rahman, *Nanomaterials*, 2022, **12**, 2122.
125 A. Fkiri, M. A. Saidani, A. Chmangui and L. S. Smiri, *J. Inorg. Organomet. Polym. Mater.*, 2023, **33**, 2523–2530.
126 D. Song, L.-W. Ma, B. Pang, R. An, J.-H. Nie, Y.-R. Guo and S. Li, *Int. J. Mol. Sci.*, 2023, **24**, 1577.
127 I. Kim, K. Viswanathan, G. Kasi, S. Thanakkasaranee, K. Sadeghi and J. Seo, *Food Rev. Int.*, 2022, **38**, 537–565.
128 C.-C. Lee, Y.-H. Lin, W.-C. Hou, M.-H. Li and J.-W. Chang, *Int. J. Environ. Res. Public Health*, 2020, **17**, 6088.
129 J.-H. Lee, G.-S. Lee, E.-N. Park, D.-H. Jo, S.-W. Kim and H.-C. Lee, *Materials*, 2023, **16**, 2099.
130 I. Rabani, S.-H. Lee, H.-S. Kim, J. Yoo, S. Hussain, T. Maqbool and Y.-S. Seo, *J. Environ. Chem. Eng.*, 2021, **9**, 105845.
131 M. Tondey, A. Kalia, A. Singh, G. S. Dheri, M. S. Taggar, E. Nepovimova, O. Krejcar and K. Kuca, *Agronomy*, 2021, **11**, 729.
132 M. A. Nazir, M. Hasan, G. Mustafa, T. Tariq, M. M. Ahmed, R. G. Dehno and M. Ghorbanpour, *Sci. Rep.*, 2024, **14**, 13091.
133 G. H. AbdElAziz, A. El-Rahman, A. Lamyaa, S. S. Ahmed, S. E. M. Mahrous and J. Soil, *Sci. Agric. Eng.*, 2021, **12**, 573–582.
134 H. Zhang, X. Zhao, J. Bai, M. Tang, W. Du, Z. Lv, K. H. M. Siddique and H. Mao, *Environ. Sci. Nano*, 2024, **11**, 351–362.
135 Z. Mazhar, J. Akhtar, A. Alhodaib, T. Naz, M. I. Zafar, M. M. Iqbal, H. Fatima and I. Naz, *Sci. Rep.*, 2023, **13**, 2022.
136 K. Elumalai and S. Velmurugan, *Appl. Surf. Sci.*, 2015, **345**, 329–336.
137 A. M. Pillai, V. S. Sivasankarapillai, A. Rahdar, J. Joseph, F. Sadeghfar, K. Rajesh and G. Z. Kyzas, *J. Mol. Struct.*, 2020, **1211**, 128107.
138 J. B. Kavya, M. Murali, S. Manjula, G. L. Basavaraj, M. Prathibha, S. C. Jayaramu and K. N. Amruthesh, *J. Drug Deliv. Sci. Technol.*, 2020, **60**, 101982.
139 R. Lahoti and D. Carroll, *Next Res.*, 2025, 100164.
140 S. Faisal, H. Jan, S. A. Shah, S. Shah, A. Khan, M. T. Akbar, M. Rizwan, F. Jan, A. Wajidullah and N. Akhtar, *ACS Omega*, 2021, **6**, 9709–9722.
141 Y. Bin Chan, M. Aminuzzaman, M. K. Rahman, Y. F. Win, S. Sultana, S.-Y. Cheah, A. Watanabe, L. S. Wong, S. K. Guha and S. Djearamane, *Green Process. Synth.*, 2024, **13**, 20230251.
142 G. Kamarajan, D. B. Anburaj, V. Porkalai, A. Muthuvel and G. Nedunchezhian, *J. Niger. Soc. Phys. Sci.*, 2022, **892**.
143 M. H. Shabani, A. Jafari, M. Manteghian and S. M. Mousavi, *Sci. Rep.*, 2024, **14**, 29409.
144 M. Saravanan, V. Gopinath, M. K. Chaurasia, A. Syed, F. Ameen and N. Purushothaman, *Microb. Pathog.*, 2018, **115**, 57–63.
145 K. Prasad and A. K. Jha, *Nat. Sci.*, 2009, **1**, 129.
146 N. Rajabairavi, C. S. Raju, C. Karthikeyan, K. Varutharaju, S. Nethaji, A. S. H. Hameed and A. Shajahan, in *Recent Trends in Materials Science and Applications: Nanomaterials, Crystal Growth, Thin Films, Quantum Dots, & Spectroscopy (Proceedings ICRTMSA 2016)*, Springer, 2017, pp. 245–254.
147 G. Baskar, J. Chandhuru, K. S. Fahad and A. S. Praveen, *Asian J. Pharm. Technol.*, 2013, **3**, 142–146.
148 B. Balraj, N. Senthilkumar, C. Siva, R. Krithikadevi, A. Julie, I. V. Potheher and M. Arulmozhi, *Res. Chem. Intermed.*, 2017, **43**, 2367–2376.
149 R. M. Tripathi, A. S. Bhadwal, R. K. Gupta, P. Singh, A. Shrivastav and B. R. Shrivastav, *J. Photochem. Photobiol., B*, 2014, **141**, 288–295.
150 E. L. Irede, R. F. Awoyemi, B. Owolabi, O. R. Aworinde, R. O. Kajola, A. Hazeez, A. A. Raji, L. O. Ganiyu, C. O. Onukwuli and A. P. Onivefu, *RSC Adv.*, 2024, **14**, 20992–21034.
151 M. Parashar, V. K. Shukla and R. Singh, *J. Mater. Sci. Mater. Electron.*, 2020, **31**, 3729–3749.
152 Y. Fang, X. Wen, S. Yang, Q. Pang, L. Ding, J. Wang and W. Ge, *J. Sol-Gel Sci. Technol.*, 2005, **36**, 227–234.
153 J. E. Rodriguez-Paez, A. C. Caballero, M. Villegas, C. Moure, P. Durán and J. F. Fernández, *J. Eur. Ceram. Soc.*, 2001, **21**, 925–930.
154 A. Dev, S. Kar and S. Chaudhuri, *J. Nanosci. Nanotechnol.*, 2007, **7**, 2778–2784.
155 J. K. Salem and T. M. Hammad, *J. Mater. Sci. Eng*, 2009, **3**, 38–43.
156 G. Otis, M. Ejgenberg and Y. Mastai, *MDPI Stays Neutral with Regard to Jurisdictional Claims in Published*, 2021.
157 M. Swain, D. Mishra and G. Sahoo, *Discov. Appl. Sci.*, 2025, **7**, 997.
158 D. Mutukwa, R. Taziwa and L. E. Khotseng, *Nanomaterials*, 2022, **12**, 3456.

159 H. Hameed, A. Waheed, M. S. Sharif, M. Saleem, A. Afreen, M. Tariq, A. Kamal, W. A. Al-Onazi, D. A. Al Farraj and S. Ahmad, *Micromachines*, 2023, **14**, 928.

160 P. Papolu and A. Bhogi, *Mater. Today Proc.*, 2023, **92**, 924–927.